An Assessment of Body Force Representations for Compressor Stall Simulation

by

Jonathan Kerner

Submitted to the Department of Aeronautics and Astronautics
in partial fulfillment of the requirements for the degree of

Master of Science in Aeronautics and Astronautics

at the

MASSACHUSETTS INSTITUTE OF TECHNOLOGY

February 2010

Author .....
Department of Aeronautics and Astronautics
February 1, 2010

Certified by .....
Edward M. Greitzer
H.N. Slater Professor of Aeronautics and Astronautics
Thesis Supervisor

Certified by .....
Choon S. Tan
Senior Research Engineer
Thesis Supervisor

Accepted by .....
Eytan H. Modiano
Associate Professor of Aeronautics and Astronautics
Chair, Committee on Graduate Students

An Assessment of Body Force Representations for Compressor Stall Simulation

by

Jonathan Kerner

Submitted to the Department of Aeronautics and Astronautics
on February 1, 2010, in partial fulfillment of the
requirements for the degree of
Master of Science in Aeronautics and Astronautics

Abstract

This thesis examines an axial compressor body force representation constructed from 3D CFD calculations. The radial distribution of body forces is compared to that of a body force representation based on axisymmetric streamline curvature (SLC) calculations, and shown to be in qualitative agreement except in the vicinity of the blade tip. In terms of stall inception type and stall point, computations based on both representations exhibit agreement with rig test data. A parametric study is undertaken in which the magnitude of the forces in the blade tip region of both representations is reduced so as to obtain reductions in compressor pressure rise similar to those observed experimentally due to increased tip clearance. It is shown that on a back-to-back basis, a given change to the end wall forces produces similar effects on the computed stall point, whether the underlying body force representation derives from 3D CFD or SLC. Based on this result one route to capturing effects of tip clearance on stall prediction can be the development of a tip clearance body force model for use in conjunction with SLC calculations.

Thesis Supervisor: Edward M. Greitzer
Title: H.N. Slater Professor of Aeronautics and Astronautics

Thesis Supervisor: Choon S. Tan
Title: Senior Research Engineer

Contents

List of Figures

List of Tables

Chapter 1

Compressor Body Force Representations for Stall Simulation

1.1 Introduction

This thesis describes a compressor body force representation developed from 3D CFD. It builds on work conducted at the MIT Gas Turbine Lab from 1999 through 2009 exploring compressor body force representations for stall simulation. References [3], [4], [8], [10] and [6] constitute this body of work. The overall goal of this effort is to develop a predictive tool for stall onset which is able to take as an input compressor geometry and to produce as an output the stall point and the stall inception type for a compressor. This chapter summarizes the progression of body force representations charted by each of the previous works, highlighting the relevant findings in each study that motivate the present work.

1.2 Rotating Stall Inception Background

Two distinct routes to rotating stall have been identified and described in the literature: spike inception and modal inception [1]. Spike inception is a short-wavelength

(compared to the circumference of the compressor) disturbance that grows rapidly into a rotating stall. Modal inception is a long-wavelength (wavelength of magnitude equal to the circumference) undulation that appears before the formation of a discrete rotating stall cell. Examples of both types of inception are shown in Figure 1-1. The plots show hot wire traces around the circumference of a compressor undergoing spike (upper panel) and modal (lower panel) stall inception. The abscissa is time in rotor revolutions and the ordinate is the hot wire output at locations around the circumference. In the case of spike inception, a narrow disturbance grows rapidly into a rotating stall cell. Modal inception occurs via a long-wavelength, small-amplitude disturbance that precedes the development of a rotating stall cell.

It has been found that the inception type for a particular compressor depends upon the occurrence of the critical rotor incidence [1]. If the critical rotor incidence occurs before the peak pressure rise characteristic on the compressor speed line (i.e. at an operating point on the negatively sloped part of the characteristic), spike type stall inception will occur. If the peak pressure rise operating point precedes the point of critical rotor incidence (i.e. critical rotor incidence occurs at an operating point on the positively sloped part of the characteristic), modal type inception will occur. In other words, if a compressor stalls while on the negatively sloped part of the characteristic, it will typically stall via spike inception; if it stalls after achieving peak pressure rise (on the positively sloped portion of the characteristic), it will typically stall via modal inception. Experimental data and a schematic diagram illustrating this point is shown in Figure 1-2. The upper panel shows experimental data in which spike and modal stall inception were observed. The abscissa is the flow coefficient, and the ordinate is the total-to-static pressure rise coefficient. Spike inception occurred at operating points on the negatively sloped portion of the characteristic. Modal inception occurred on the positively sloped portion of the characteristic. This is explained by the point of critical rotor incidence, as shown on the total-to-static pressure rise characteristics in the lower panels.

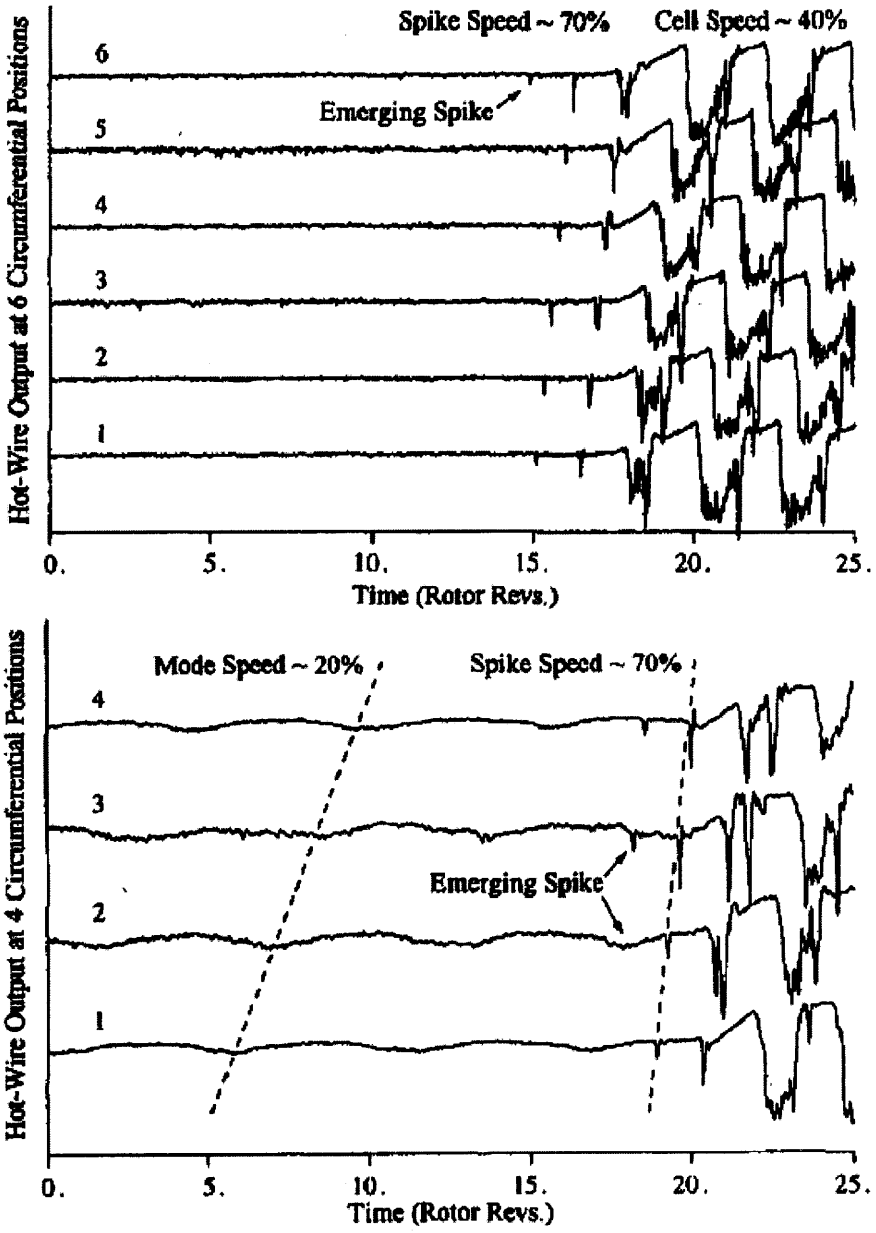

Figure 1-1: Typical spike and modal stall inception [1]

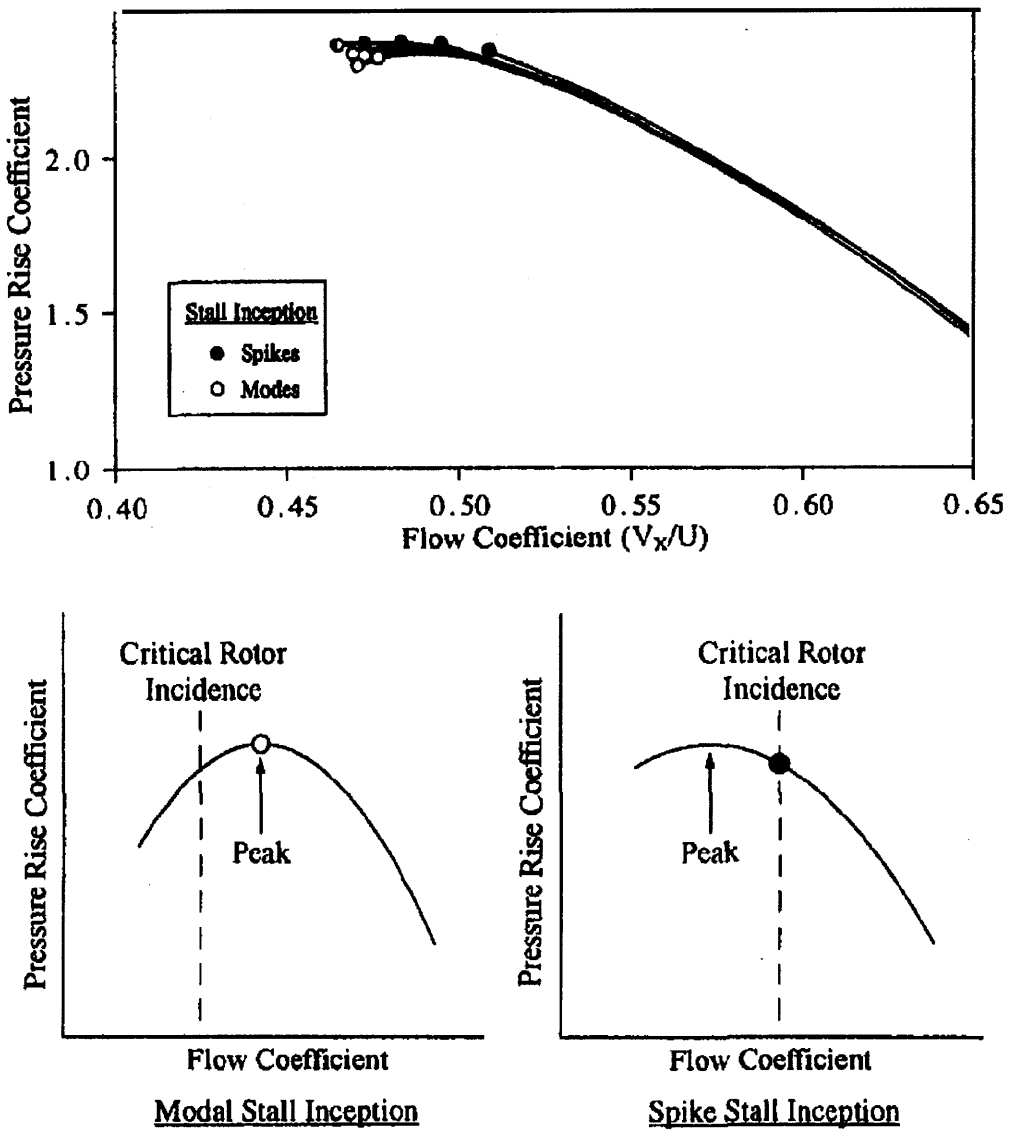

Figure 1-2: Dependence of stall inception type on occurrence of critical rotor incidence [1]

1.3 Synthesis of Prior Work

[3], [4], [8], [10] and [6] represent different evolutions of the approach to representing compressors using body forces. These representations differ in fidelity and in utility. In terms of fidelity, the differences between the representations in [3] and [10] can be depicted on three axes corresponding to the fidelity of the body force magnitudes, fidelity of the axial distributions and fidelity of the radial distributions, as in Figure 1-3. The three axes in the figure correspond to the fidelity of the three primary inputs that specify a body force representation. The x-axis is the fidelity of the specified axial distribution of forces, the y-axis is the fidelity of the specified radial distribution of forces, and the z-axis is the fidelity of the specified magnitude of the forces. Each axis spans three discrete levels of fidelity. The lowest and highest fidelity corners of the space are marked as such. Three *(x,y,z)* points corresponding to the three body force representations discussed in this thesis are plotted. The body force representation developed from 3D CFD presented in this thesis represents an increase in input fidelity relative to the representations in [3] and [10].

Gong's [3] body force representation incorporates force magnitudes specified *a priori* taken from a defined pressure rise characteristic. A uniform radial distribution is used, and the axial distribution in each blade row is assumed to be a smooth curve varying from zero at the leading edge to a peak at mid-chord and back down to zero at the trailing edge.

Walker [10] employed force magnitudes and radial distributions extracted from streamline curvature (SLC) calculations. 2D cascade calculations were used for the axial distribution of forces in [10]. The aim of this thesis is to investigate the next higher fidelity body force representation which is developed directly from 3D CFD calculations, with minimal assumptions required to compute stall onset.

In addition to differences in fidelity, there is also a difference in utility between the approaches in [3] and [10]. The basis for the body force representation in [10] is compressor geometry, whereas the basis for that in [3] is a compressor pressure rise characteristic. The latter is thus linked only to the assumed pressure rise versus

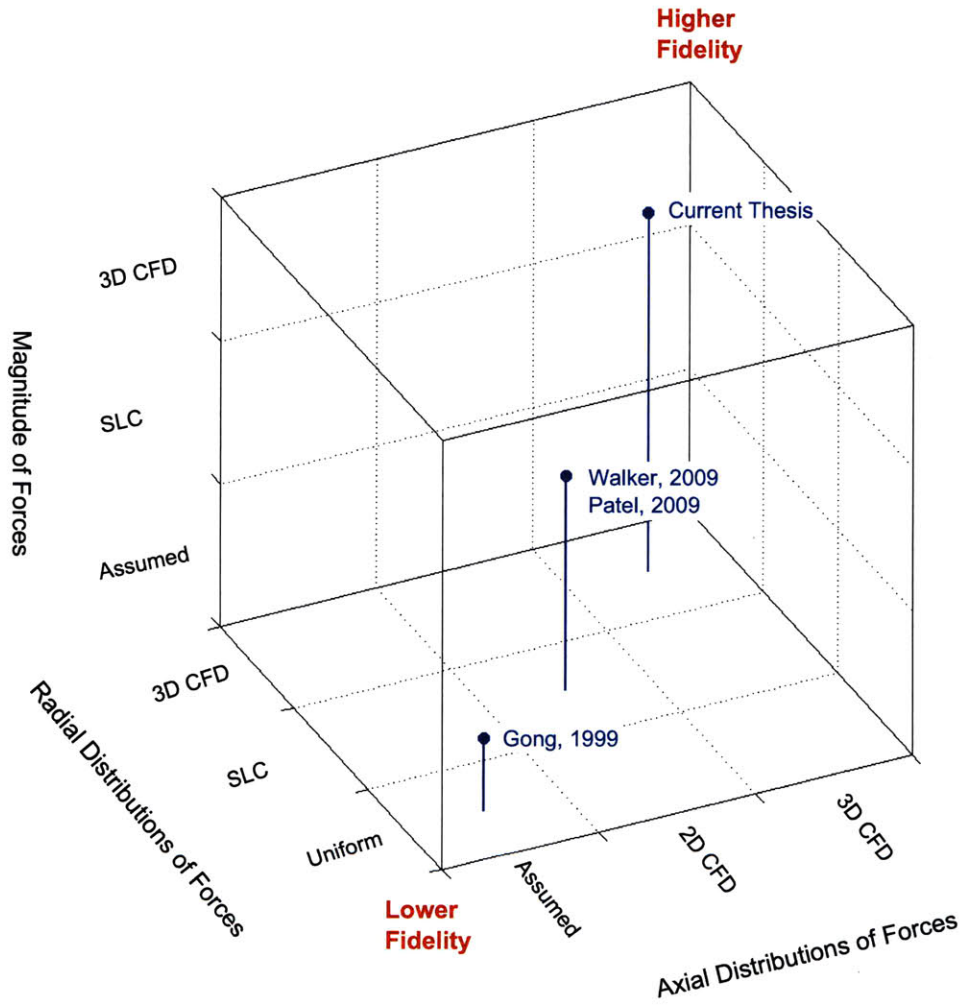

Figure 1-3: Depiction of the differences in fidelity of body force representations

flow behavior of a hypothetical compressor design, for which geometry need not be specified. One or the other approach may offer increased utility, depending on the application. The current thesis extends the approach in [10] in that the compressor geometry is required as an input for CFD calculations, from which the forces are extracted.

Kiwada [4] and Reichstein [8] contributed enabling methodologies for body force estimation. A procedure to compute body forces from a specified flow field is described in [4]. This procedure was used in [10] in concert with CFD calculations to generate body forces for a given compressor geometry. A means of linking body forces and flow field features is discussed in [8].

Patel [6] also contributed to the use of the body force representation discussed herein. In [6], it was shown that for representations based on 3D CFD, the local force cannot be specified solely as a function of the local flow coefficient, ϕ, as was done in [3] and [10]. It was found that the relationship between local flow coefficient and overall flow coefficient was not monotonic for 3D CFD solutions at successive operating points on a compressor speed line. Hence, the value of a local force at a given local flow coefficient may be non-unique. A method whereby the local force is specified as a function of the product of the local and overall flow coefficient, termed $\phi\phi$, was shown in [6] to address this. The influence of different force versus flow rate behaviors at flows below the peak of the pressure rise characteristic was also examined.

Extensive sensitivity studies to assess the impact of various input parameters on computed stall onset are documented in [10] and [6]. The study in [10] investigated the sensitivity of computed stall inception to four primary features: the radial distribution of axial rotor body forces, the radial distribution of tangential rotor body forces, the axial distribution of rotor body forces, and the post-stall compressor characteristic (i.e., the low flow region of the pressure rise characteristic). The variation in post-stall characteristics was assessed using the lower-fidelity body force representation in [3]. The metrics examined in [10] were the computed stalling flow coefficient and the type of computed stall inception.

The results of the sensitivity study are shown in Figure 1-4. The four panels each depict (from left to right) the effect of changes to the radial distribution of axial forces, radial distribution of tangential forces, axial distribution of axial and tangential forces, and to the specified post-stall compressor characteristic. For all four panels, the ordinate depicts the percent change in stalling flow coefficient relative to the baseline representation. In the first two panels, the abscissa depicts the percent change in forces at the tip relative to the baseline representation. In [10], the changes to the radial distributions were specified as a percent change at the tip and an equal and opposite percent change at the hub, with a linear relationship between percent change and radius throughout the span. The abscissa in the third panel depicts two discrete axial distributions examined in [10], as noted. The abscissa in the fourth panel represents five discrete post-stall compressor characteristics. In each panel, the data points are color-coded to show the type of stall onset ('slow spike'[1], spike, or modal). It is evident that out of the four inputs examined in [10], the stalling flow coefficient is most sensitive to changes in the radial distribution of axial forces.

A limited assessment of sensitivity to the magnitude of the forcing perturbation is also documented in [10], as noted in the first panel in Figure 1-4. It was found that reducing the forcing magnitude to a value equal to 1 percent of that in the baseline case changed the stall inception from 'slow spike' to modal.

The use of the $\phi\phi$ variable was shown in [6] to change the stalling flow coefficient by approximately 15 percent relative to the same calculation using the ϕ variable. The stall inception type obtained in [6] using the $\phi\phi$ variable differed from that in [10] using ϕ; it was shown that the input perturbation grew into a rotating part-span disturbance within approximately 1 rotor revolution (a classic spike stall), whereas a 'slow spike' was reported in [10].

The work in [6] is best understood as an enabling step toward the use of a higher fidelity body force representation. It was found that variations in the stalling flow coefficient of up to approximately 15 percent are possible, depending on the form

[1]'Slow spike' is the term used in [10] to describe stall onset in which the input perturbation is sustained for several rotor revolutions, then appears to die out, and finally reappears after several rotor revolutions as a rotating part-span disturbance

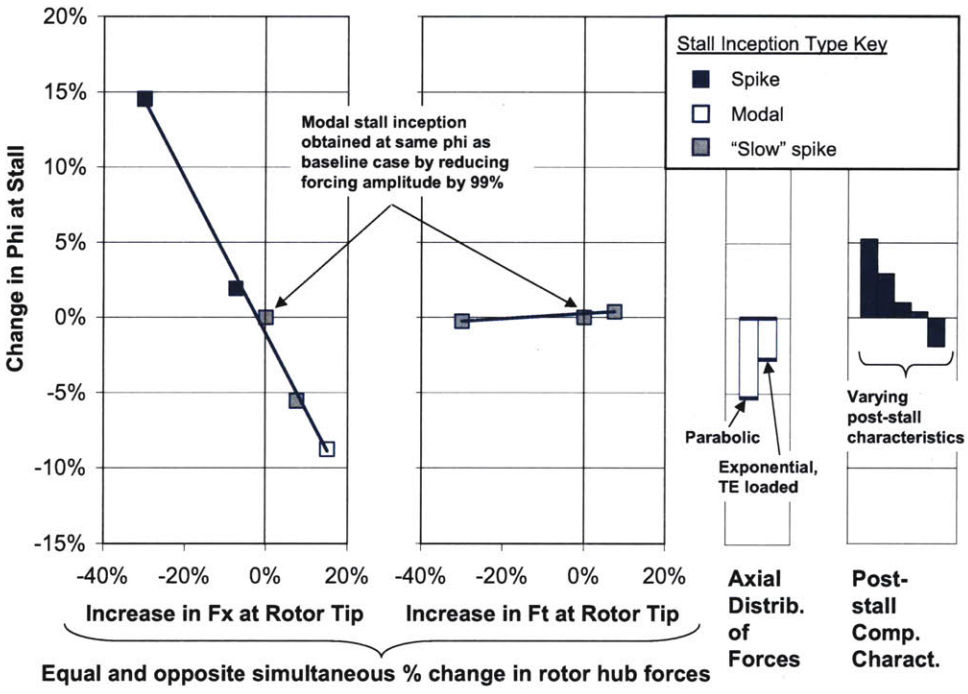

Figure 1-4: Summary of results from sensitivity study in [10]

assumed for the body force magnitudes at flows below the peak [7]. Spike and modal stall inception were obtained in some cases. No stall was obtained in others. These results suggest that the calculated stall onset is more sensitive to body force characteristics at low flows for a higher fidelity body force representation than implied by the lower fidelity body force representation in [3].

1.4 Motivations for the Current Thesis

A key result from the study in [10] is that the radial distribution of axial forces has a strong effect on stall inception. This result is one motivator for development of a body force representation extracted from 3D CFD calculations. In this regard, 3D CFD can (theoretically) capture end wall effects without any *a priori* knowledge of their form. Further, the end wall effects can produce radial distributions that are different from those computed by SLC methods. Hence it is the aim of this study to describe the body forces derived from 3D CFD and assess the effect of radial distributions of these forces on computed stall inception. In particular, the methods developed to date are limited in their ability to account for the effect of blade tip clearance on computed stall onset. The work presented in this thesis addresses this limitation.

1.5 Thesis Contributions

This thesis contributes three new developments on the subject of compressor body force representations for stall simulation. The first is the demonstration of stall simulations using a compressor body force representation developed from 3D CFD calculations. These simulation results are presented alongside the results from [10] for a back-to-back comparison with stall simulation using body forces extracted from SLC. The second contribution is a method for assessing the effect of changes to local forces in a given body force representation. This method provides a means of capturing in a self-consistent manner the effect of changes to the local flow due to changes to local forces. The third contribution is an assessment of the effect of

changes in end wall forces on the computed stall onset. The magnitude of forces in the blade tip region is reduced in order to obtain effects on the computed compressor pressure rise characteristic similar to those observed experimentally due to increased tip clearance, and the impact on computed stall onset is determined.

Chapter 2

Baseline Body Force Representation and Computed Stall Onset

2.1 Objective

This chapter describes a body force representation based on 3D CFD calculations (hereafter termed the 'baseline' body force representation). Stall onset simulation results based on the baseline representation are presented and compared to test data and to the simulation results in [10] and [6].

2.2 3D CFD Calculations

Unsteady, multi-blade passage 3D CFD solutions were computed at several operating points along a compressor speed line, from design to a point near the peak of the characteristic. Denton's TBLOCK [2] was used for these calculations. The geometry was a single stage low-speed compressor whose performance and stall onset characteristics were measured in rig testing carried out prior to this study (as such, the computations presented in this thesis are postdictions, not predictions). A sketch of the compressor configuration and the CFD mesh is shown in Figure 2-1. The upper

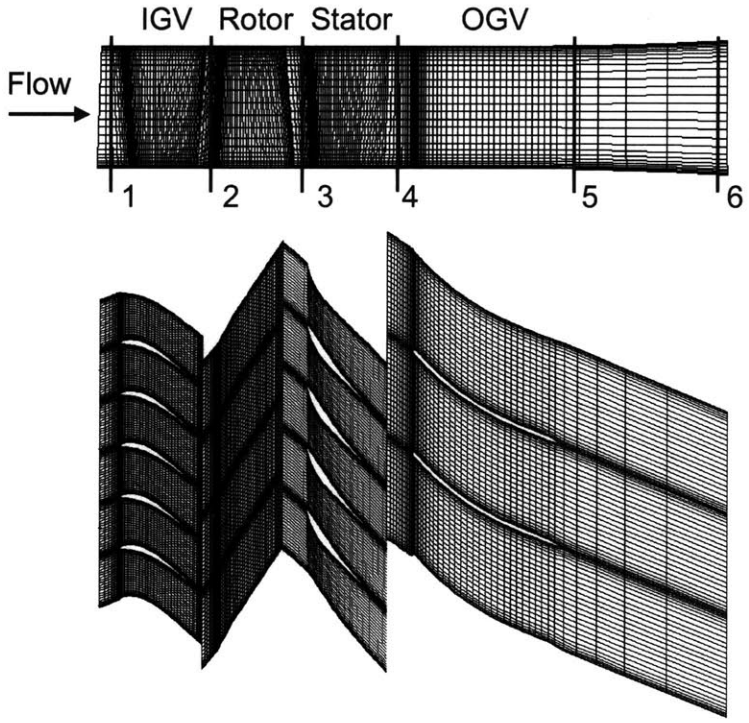

Figure 2-1: Meridional and blade passage view at casing of TBLOCK grid

panel shows a meridional view of the 3D CFD grid used for this study, with annotations denoting the axial stations upstream and downstream of each blade row (these station locations are referenced in subsequent figures and tables). The lower panel shows a blade passage view of the grid at the casing. As shown, this grid includes multiple blade passages for each blade row and the full blade geometry. The grid also includes a tip clearance gap at the rotor casing.

A comparison of the TBLOCK and test data speed lines is given in Figure 2-2. In this plot and all other pressure rise and flow coefficient results presented in this thesis, the values given are normalized by the pressure rise coefficient at design and flow coefficient at design, respectively. The abscissa in this figure is the overall flow coefficient. The ordinate is static pressure rise coefficient at the stator exit, relative to the inlet total pressure. The rig test and CFD speed lines are shown along with

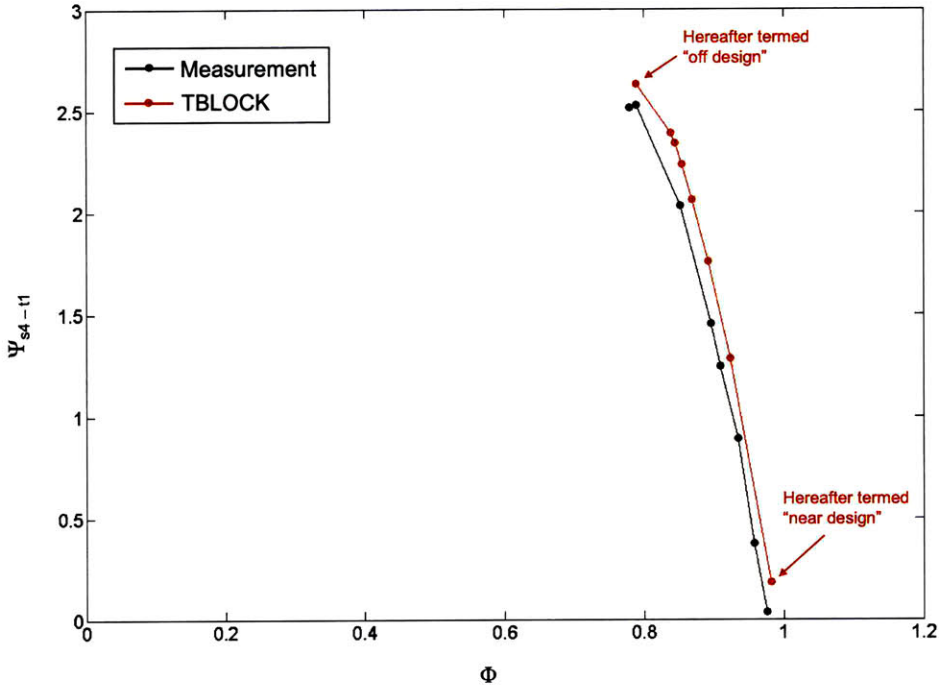

Figure 2-2: Comparison of TBLOCK results to test data

annotations denoting the design and off-design operating points referenced throughout this thesis. The CFD pressure rise characteristic exhibits good agreement with the measured data.

2.3 Body Force Distributions

The results of the TBLOCK calculations were processed using the force extraction procedure in [4] to obtain the local force as a function of $\phi\phi$ for each cell in the computational domain. These forces, directly extracted from the CFD solutions without any modifications, are hereafter termed 'raw' because the subsequent body force representation for the baseline stability calculation and those for the end wall force sensitivity study incorporate various modifications. Plots of the raw rotor forces are shown in

Figures 2-3 and 2-4, with annotations showing the spanwise location of the blade tip. In pseudocolor plots showing the distributions of local forces, the scale corresponds to force per unit mass times the inverse of the mean wheel speed squared. In plots showing the chordwise integrated force distributions, these local forces are multiplied by the length of the corresponding computational cells, which results in units of non-dimensional force. These units are used consistently throughout this thesis.

Figure 2-3 depicts the rotor axial force distributions extracted from the 3D CFD calculations at the design operating point. The left panel shows a meridional pseudocolor plot of the axial force distribution in the rotor (the abscissa is the chord and the ordinate is the span, the colors correspond to units of non-dimensional force per unit length). The right panel shows the chordwise integrated value (abscissa) computed from this same distribution at each spanwise location (ordinate) in the rotor. In both panels, the spanwise location of the blade tip is denoted by a horizontal black line. The pseudocolor plots show there is a small radial gradient in axial forces throughout the span, with the exception of the tip clearance gap where a large gradient is present. Axially, the the distributions are leading edge loaded. The integrated axial force varies smoothly from a minimum value at the hub to a local maximum near the blade tip, with a sharp peak in the tip clearance gap. The maximum integrated value of the axial forces occurs in the tip clearance gap.

Figure 2-4 depicts the rotor tangential force distributions extracted from the 3D CFD calculations at the design operating point. The distribution is qualitatively similar to the axial distribution in that it is leading edge loaded, with a large radial gradient present near the blade tip. Likewise, the maximum chordwise-integrated value occurs in the tip gap.

Figures 2-3 and 2-4 show the forces in the blade tip clearance gap as comparable in magnitude to the forces at the blade tip. In fact, the largest chordwise integrated force occurs in the tip gap. These large forces are caused by an apparent momentum flux through the casing wall due to non-zero radial velocities at the casing present in the TBLOCK solutions. The computed large tip gap forces are not seen as realistic

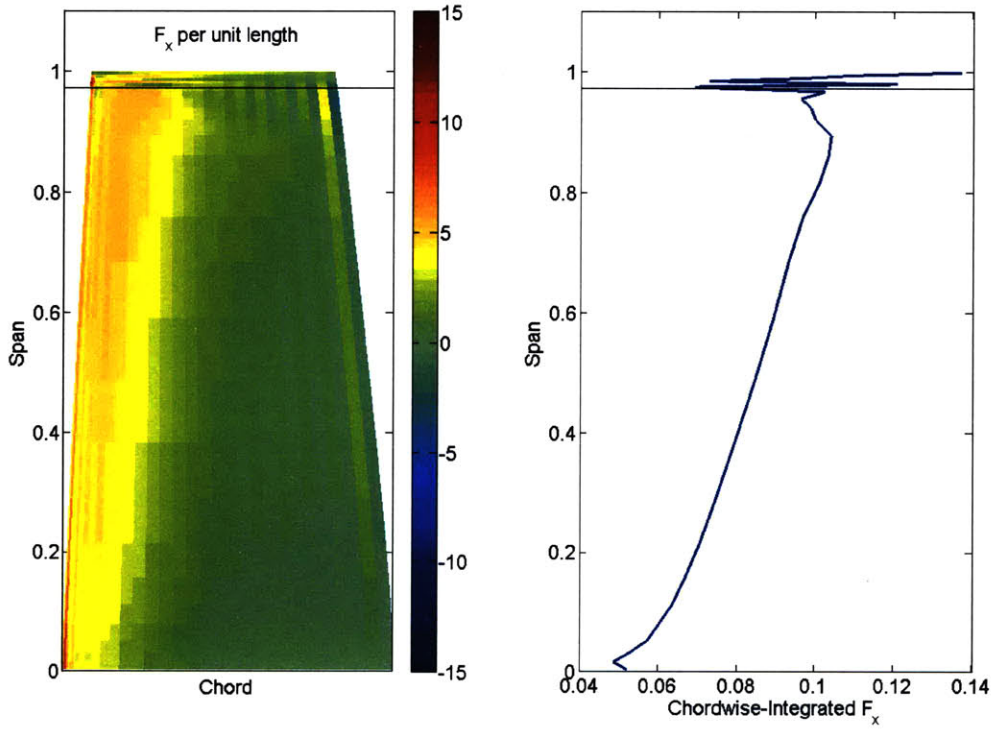

Figure 2-3: Raw TBLOCK axial force distributions

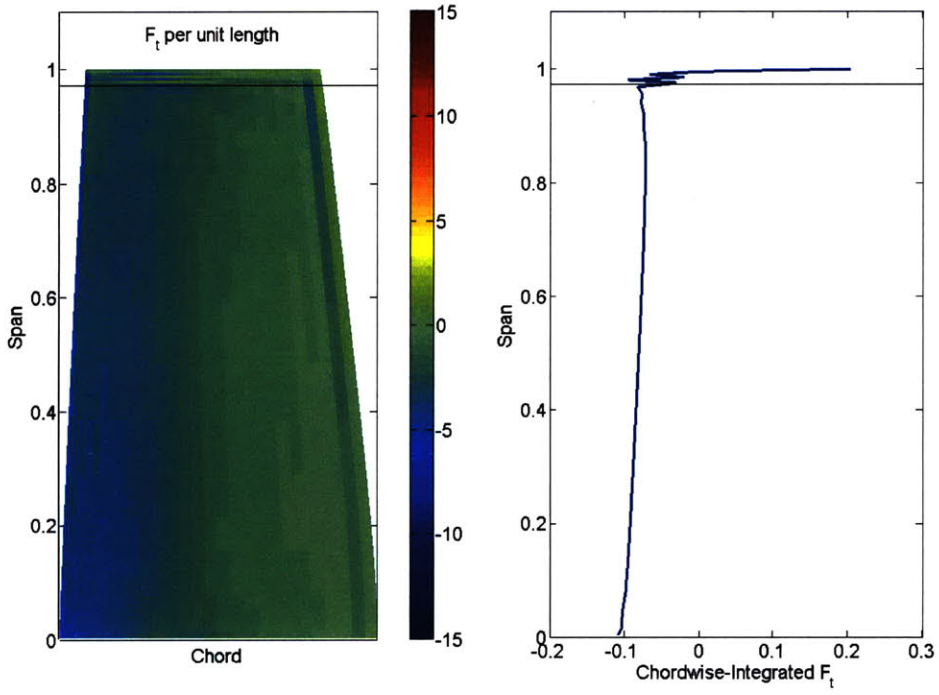

Figure 2-4: Raw TBLOCK tangential force distributions

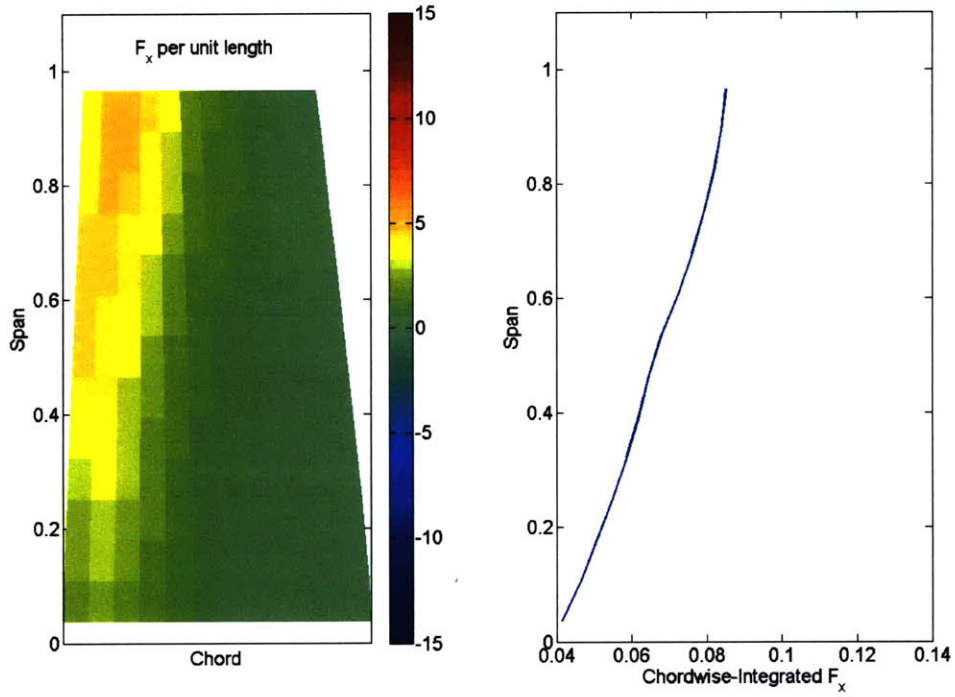

Figure 2-5: SLC axial force distributions

and it is believed that the forces in the tip gap are not larger in magnitude in the aggregate than those at the blade tip. This assertion is given some justification by the results of the end wall force sensitivity study (see 3.3), in that the trends with increasing tip clearance observed in the test data are captured by specifying tip gap forces that are successively smaller in magnitude than those at the blade tip. The SLC-based axial forces and tangential forces in [6] are shown in Figures 2-5 and 2-6, respectively.

Figure 2-5 depicts the rotor axial forces extracted from SLC at the design operating point. The sharp gradients in the TBLOCK distributions near the blade tip are not present in the SLC distributions; the SLC and TBLOCK datasets otherwise exhibit good qualitative agreement in terms of overall trends in the axial and radial distributions. The same is true of the rotor tangential forces extracted from SLC at

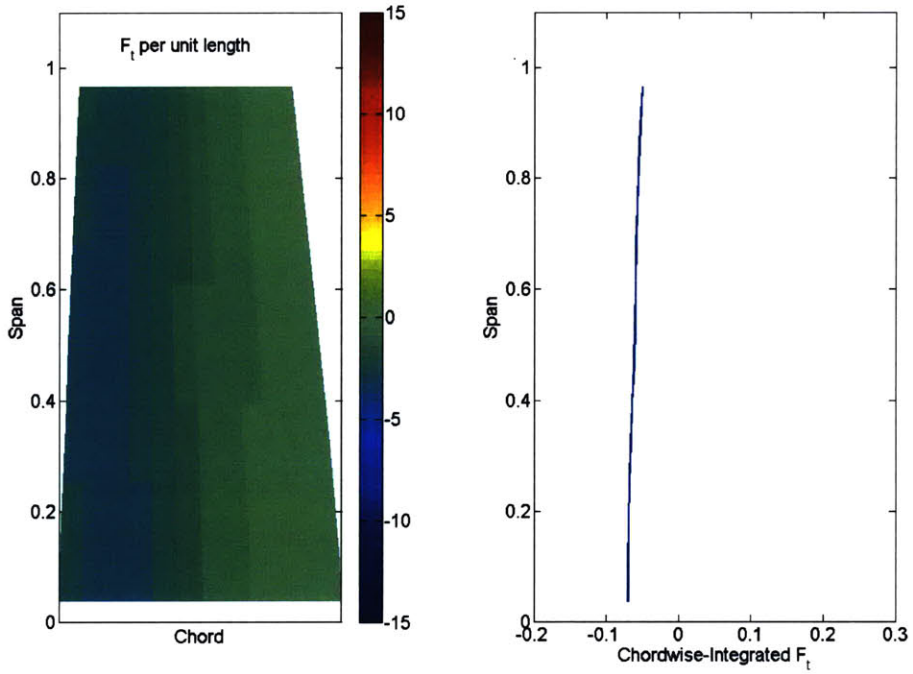

Figure 2-6: SLC tangential force distributions

the design operating point, as shown in Figure 2-6.

Qualitatively, the raw TBLOCK force distributions resemble the SLC force distributions with the exception of the forces in the tip gap.[1] That observation, combined with the overall agreement between the TBLOCK and test data speed lines, suggests that though the raw forces in the tip gap may be spurious, those elsewhere in the domain are good representations of the actual forces.

2.4 Assumed End Wall Forces

To examine the effect of end wall forces we have proceeded based on the following assumptions. First, the magnitude of the chordwise integrated forces at the blade tip

[1]Though not shown, similar trends are present in the off-design distributions.

is taken to represent an upper bound on the magnitude of the chordwise integrated forces in the tip clearance gap. For a 'baseline' body force representation in this parametric examination, we thus assumed the forces in the tip clearance gap were equal in magnitude and distribution to the forces at the blade tip. In terms of implementation, this was accomplished by utilizing the forces at the blade tip throughout the spanwise region from the blade tip to the casing. The raw forces elsewhere in the span were left unchanged.

A comparison of raw and baseline rotor forces is shown in Figure 2-7. The figure presents, in the same format as Figure 2-3, the assumed rotor axial forces for the outer 20 percent span (the forces in the spanwise extent from the hub to the blade tip are identical to those shown in Figure 2-3). The forces in the spanwise extent from the blade tip to the casing are assumed to be the same as the forces at the blade tip shown in Figure 2-3. The resulting force distributions exhibit good qualitative agreement with the SLC forces shown in Figures 2-5 and 2-6 throughout the entire span. After incorporating the assumed forces in the end wall region, the maximum chordwise-integrated axial and tangential forces occur below the tip.

2.5 Link Between Local Force and Local Flow

A given body force representation not only includes the force magnitudes and distributions throughout each blade row, but also establishes an explicit relationship between local force and local flow. This relationship is a functional dependence of local force magnitude on either the local flow coefficient or the product of the local and overall flow coefficients (see [6] for more detail). Said differently, the model is that of a one-to-one correspondence between local force and the flow reference parameter. Hence a modification to a local force implies a modification to the local flow. The quantitative effect of a given force modification on the local flow is not known *a priori*, so a means of determining its impact is required to implement the end wall force assumptions mentioned above in a self-consistent manner.

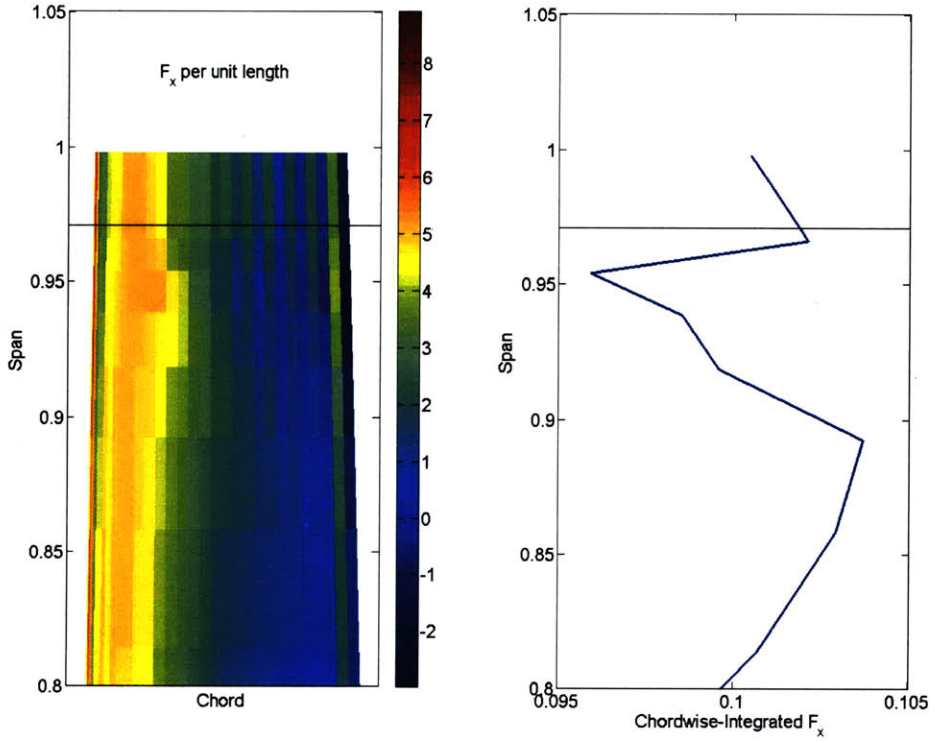

Figure 2-7: Assumed force distributions in outer 20 percent span

2.6 'Force-Flow Reconciliation'

To establish a self-consistent link between the local forces and flows for the baseline body force distribution, a method of determining the flow field that corresponds to the baseline force field was developed. This method, termed 'force-flow reconciliation' produces a flow field at a specified operating point that is consistent with a given set of forces.

The force-flow reconciliation procedure uses as an input a force field that varies spatially, but is invariant with flow. The magnitude and direction of the input forces can vary within each blade row, but the magnitude and direction at any given location do not vary with changes in the local or global flow. The output of the force-flow reconciliation procedure is a flow-field that is consistent with the input force field. The existing procedure for establishing the relationship between local forces and local flows is described below:

1. Generate CFD solutions

   CFD solutions are obtained at several operating points on a compressor speed line.

2. Extract forces

   Each solution is flux-averaged in time and theta, then analyzed using the control volume approach in [4] to extract the force distributions.

3. Establish dependence of force on flow

   For each operating point, each local force is linked in 'look-up' fashion to the corresponding local flow parameter (either ϕ or $\phi\phi$).

4. Concatenate forces and flows from all available operating points

   The final step is to concatenate forces and flows from all available operating points. The information from all of the operating points is combined to define the functional dependence of force on flow for each location in each blade row.

If the raw forces were to be modified, the desired modifications would be made after step 2 above. Before proceeding to step 3, the force-flow reconciliation procedure would be performed n times for operating points 1 through n using the modified forces at each operating point. The n outputs would then constitute the source for all required flow information in steps 3 and 4.

The force-flow reconciliation procedure uses UnsComp[2] to generate a flow field that corresponds to a given force field. In UnsComp, the flow is dependent on two inputs: the force field and the throttle area (the overall flow). The force field is given by the raw body forces plus the desired modifications. The throttle area is chosen such that the overall mass flow corresponds to the operating point at which the raw forces were extracted from the CFD solution. When the throttle area is determined and UnsComp converges, the force-flow reconciliation procedure concludes, and the resulting flow field is passed to Step 3. This procedure was used in this project only to incorporate localized modifications to raw forces as extracted from CFD solutions, but its potential applications may be broader. For example, if compressor blade row body forces were known *a priori*, this procedure could be used to generate corresponding local flow information required to fully define the body force representation for stability simulations.

The force-flow reconciliation procedure was carried out using the baseline force distributions. A comparison of the flow field corresponding to the raw force distributions and the flow field produced by force-flow reconciliation using the baseline force distributions is shown in Figure 2-8. The figure shows the distribution of the local flow coefficient in the rotor at the off-design operating point. In both panels, the abscissa is the chord, the ordinate the span, and the local flow coefficient is shown in a pseudocolor plot. The left and right panels show the flow field before and after force-flow reconciliation, respectively. Two features are noteworthy. First, the region of reverse flow in the vicinity of the rotor tip present in the 'before' flow field is not present in the 'after' flow field. Second, the changes present in the 'after' flow field relative to the 'before' flow field are not limited to blade tip region. This is evident

[2]UnsComp is the Euler solver discussed in [3]

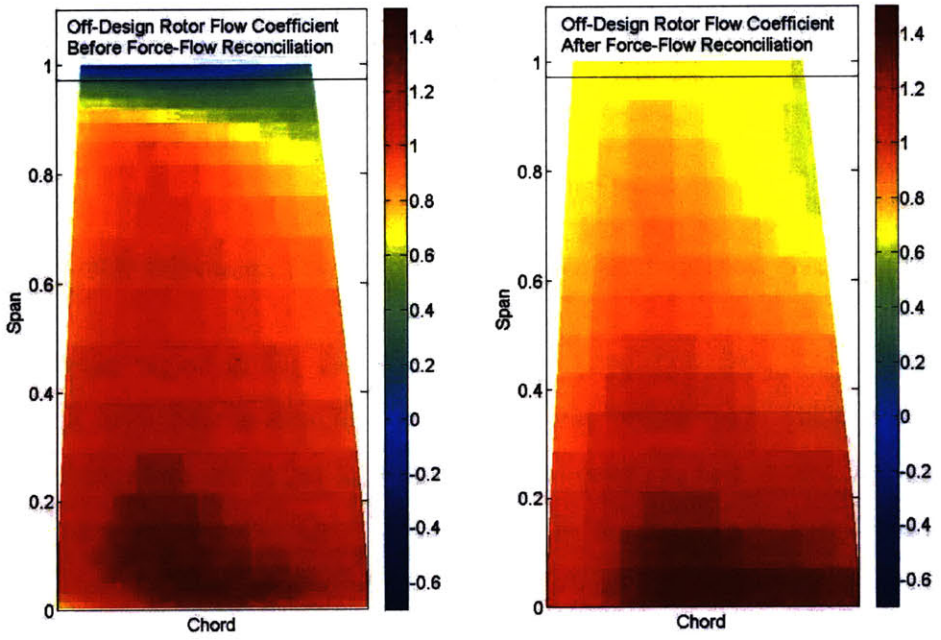

Figure 2-8: Off-design flow fields before and after force-flow reconciliation

in the midspan region in the two plots. In the 'after' flow field, the magnitude of the midspan local flow is smaller than that in the 'before' plot. This is consistent with the elimination of tip leakage flow and the constraints imposed on the force-flow reconciliation process. The overall mass flow is fixed, so with tip leakage flow no longer present in the blade tip, the flow elsewhere in the span must be reduced. This is indicative of the fact that the force-flow reconciliation process yields changes throughout the flow field even if the changes in the forces are localized.

2.7 Assumed Forces at Low Flows

In addition to force-flow reconciliation, one more step is required to fully define the baseline body force representation. The TBLOCK solutions only span the range

of flows from near-design to near-stall, and additional assumptions are required to specify body forces for the range of flows below the near stall values. The forces at these flows (basically the forces on the positive sloped part of the pressure rise characteristic) for all instability calculations discussed herein were specified by a linear dependence on flow. The force is set to a magnitude of zero at zero flow in all blade rows and is taken to vary linearly with the local flow parameter to the as-extracted magnitude at the lowest-flow CFD solution available.

The resulting force characteristic is sketched for several hypothetical cells in Figure 2-9. The abscissa in the upper panel is the overall flow coefficient, the ordinate is the pressure rise coefficient. A representative pressure rise characteristic is shown, with an annotation denoting the peak pressure rise operating point. In the lower three panels, the abscissa is the $\phi\phi$ reference variable, and the ordinate is the magnitude of the local force. Each of the lower panels shows a force characteristic for a different location in the blade row. The blue portions of the force characteristics would be constructed directly from the CFD solutions, which span the range of flows from the design operating point to the operating point at which peak pressure rise occurs. The red portions of the characteristics would be the assumed force characteristic for the range of $\phi\phi$ from a negative reference value to the value at the peak pressure rise operating point.

The justification for a linear force characteristic passing through zero force at zero flow is twofold. First, the forces at flow coefficients below the value of peak pressure are in the aggregate less than those at the peak. This is an assumption but it is seen in the relationship between force and pressure rise derived in the SLC calculations. Second, this assumption allows direct comparisons with calculations in [6] for the baseline case. An additional back-to-back assumption made here is that a linear relationship with a large negative slope defines the forces for reverse flow, as shown in Figure 2-9.

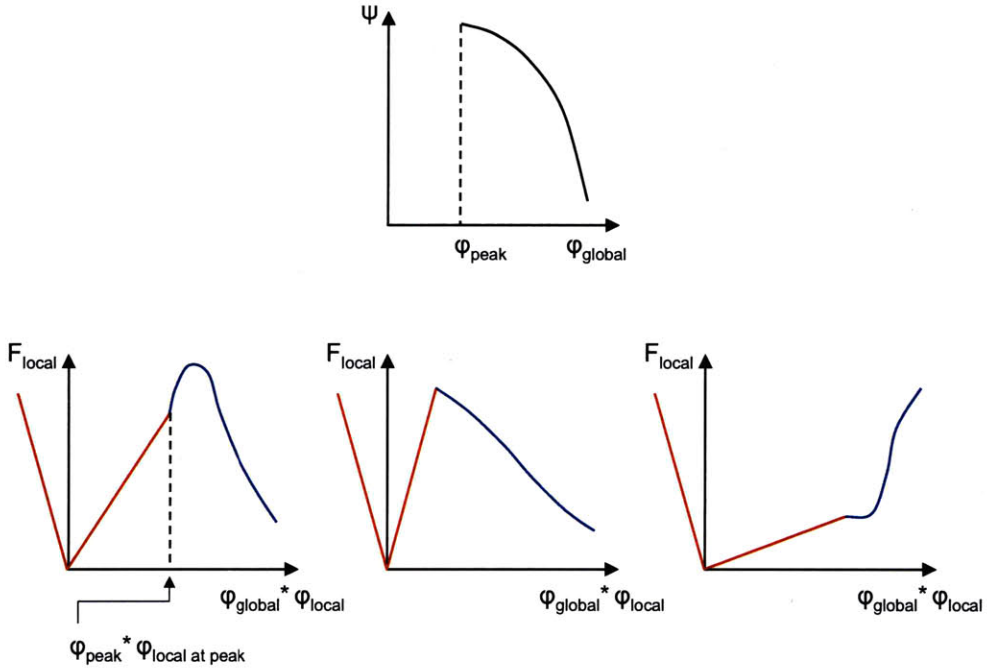

Figure 2-9: Force characteristics for three nominal locations within a blade-row.

2.8 Baseline Body Force Representation

Table 2.1 gives the specifications defining the baseline body force representation and a comparison to the SLC-based representation used in [6].

Item	Representation in [6]	Present Work Baseline
Basis for forces in the flow range from near-design to near-stall	As extracted from SLC flow fields	As extracted from TBLOCK flow fields
Basis for radial distribution of forces	As extracted from SLC flow fields	As extracted from TBLOCK flow fields
Basis for chordwise distribution of forces	As computed from 2D cascade calculations	As extracted from TBLOCK flow fields
Force modifications	None	Blade tip forces replicated throughout blade tip clearance gap
Local flow parameter to which local forces are linked	$\phi\phi$	$\phi\phi$
Consistency between local flow and local force	Assumed [a]	Enforced via force-flow reconciliation
Forces in the flow range from near-stall to zero flow	Linear relationship specified from extracted forces near stall to zero force at zero flow	Linear relationship specified from extracted forces near stall to zero force at zero flow
Forces in the flow range from zero flow to reverse flow	Linear relationship specified from zero force at zero flow to a large force for reverse flow	Linear relationship specified from zero force at zero flow to a large force for reverse flow
Metal blockage	None	Metal blockage specified throughout span
Blade rows included	IGV, Rotor, Stator	IGV, Rotor

[a] This assumption is known to materially affect the computed stall onset results. For the parametric study discussed in 3.1, force-flow reconciliation was employed for all the SLC-based cases.

Table 2.1: Comparison of body force representations

2.9 Baseline Instability Calculations

The instability calculation performed using the baseline body force representation described above is hereafter termed the 'baseline' instability calculation to distinguish it from subsequent instability calculations performed as part of the end wall force parametric study. The process for carrying out all instability calculations presented here is as follows:

1. Axisymmetric speed line calculation

   The body force representation from TBLOCK or SLC calculations is input to UnsComp running in an axisymmetric, steady mode and the throttle setting is specified to obtain a desired mass flow rate. This step is repeated at several throttle settings to generate a compressor speed line.

2. Quasi-axisymmetric instability calculation

   The flow field from an operating point on the axisymmetric speed line is used to 'seed' UnsComp in its unsteady mode (see section A.3). Once an axisymmetric solution is converged, the body forces in the rotor tip are perturbed. If the perturbation decays over time and the flow field returns to its initial state, the operating point is deemed stable. If the perturbations grow into a persistent flow field disturbance, the operating point is deemed unstable. This process is repeated at several operating points until the highest flow point at which instability occurs is identified. This point is taken as the stall point.

The UnsComp grid used for the instability calculations is the same grid used in [10] and [6] and is shown in Figure 2-10. Relative to the TBLOCK grid shown in Figure 2-1, the UnsComp grid is more coarse. In particular, the UnsComp radial grid resolution adjacent to the casing is significantly reduced relative to the TBLOCK grid. Interpolation of the force and flow fields from the TBLOCK grid to the UnsComp grid is thus required. In addition, the coarseness of the UnsComp grid in the blade tip region constrains the force variations introduced in the parametric study discussed in the next chapter.

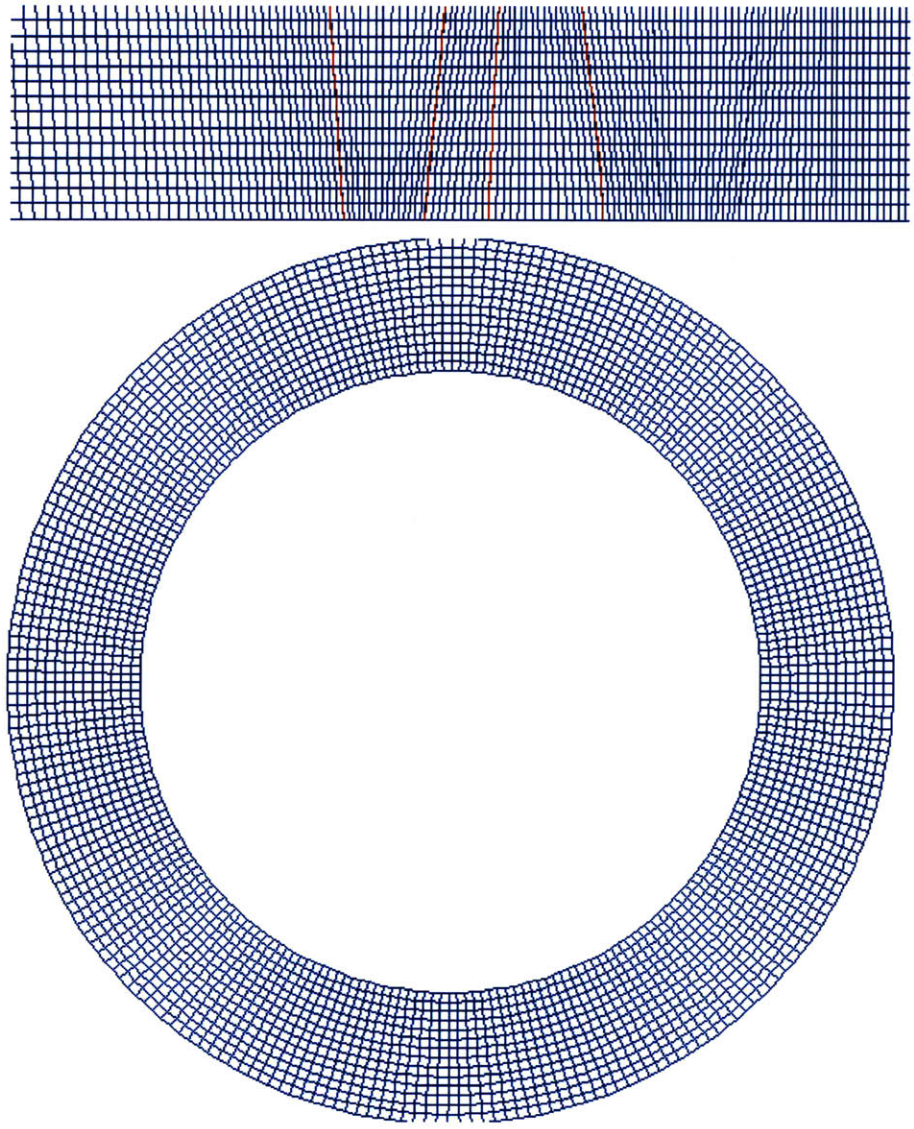

Figure 2-10: Meridional and annular views of UnsComp grid

A summary of the results from the baseline instability calculation are shown in Figure 2-11. In the right panel, the pressure rise characteristics are plotted for both the TBLOCK (red) and UnsComp (blue) calculations. The peak pressure rise TBLOCK operating point is denoted by a vertical dashed line, as is the UnsComp instability point. The upper left panel shows UnsComp unsteady traces of local flow coefficient around the casing circumference at the rotor exit at the point of instability. The time at which the perturbation is input is denoted by a vertical red line. The initial perturbation grows into a persistent rotating disturbance in about five rotor revolutions. The black vertical dashed line marks the time corresponding to the annular pseudocolor plot of the normalized local flow coefficient shown in the lower left panel, in which it is evident that the disturbance is a part-span region of low-flow encompassing about a quarter of the annulus.

Two features of the baseline instability results should be noted. First, the instability exhibits a classic spike-type onset. Second, the initial perturbation grows into a part-span disturbance that rotates around the annulus at approximately 33 percent rotor speed and appears to approach a time-invariant pattern (the simulation comes to an end when reverse flow develops at the domain exit of the computational domain).

Figure 2-12 shows a comparison of the stall onset from the baseline instability calculation to the onset pattern reported in [10] and [6] as well the onset pattern measured in rig testing.[3] Each of the panels depicts time unsteady casing traces at the rotor exit at the instability point. The results presented here are qualitatively similar to those in [6] in that they exhibit a spike-type stall onset that transitions to rotating stall. There is less agreement with the results in [10], which exhibit 'slow-spike' type stall onset. It was shown in [6] that the local flow parameter (ϕ vs. $\phi\phi$) is responsible for this difference. The stall inception, stall point and stall cell rotation speeds are summarized in Table 2.2.

[3]The rig test data consists of casing pressure tap traces; the simulation results have customarily been presented in the form of casing velocity traces and are done so here for consistency. The present work baseline velocity and pressure trace patterns are qualitatively similar and it is believed that this is also true for the results in [10] and [6]

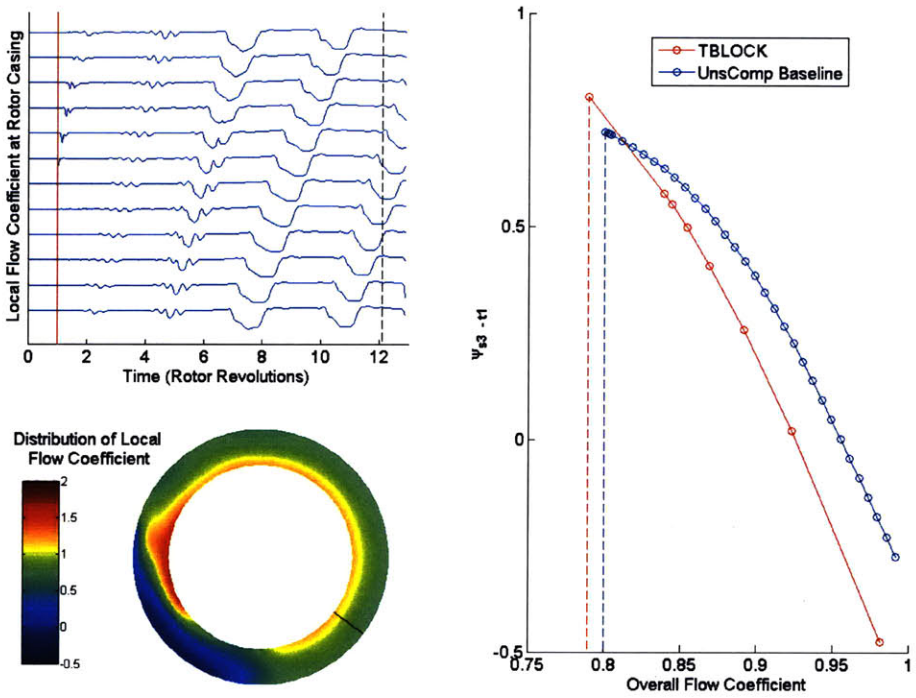

Figure 2-11: Baseline instability simulation results

	Present Work Baseline	**Results in [10]**	**Results in [6]**	**Rig Test**
Stall onset type	Spike	Slow-spike	Spike	Spike
Stalling flow coefficient	0.800	0.802	0.678	0.780
Approx. $\Omega_{wheel}/\Omega_{cell}$	0.33	0.67	0.67	0.67

Table 2.2: Comparison of stall onset simulation and rig test metrics

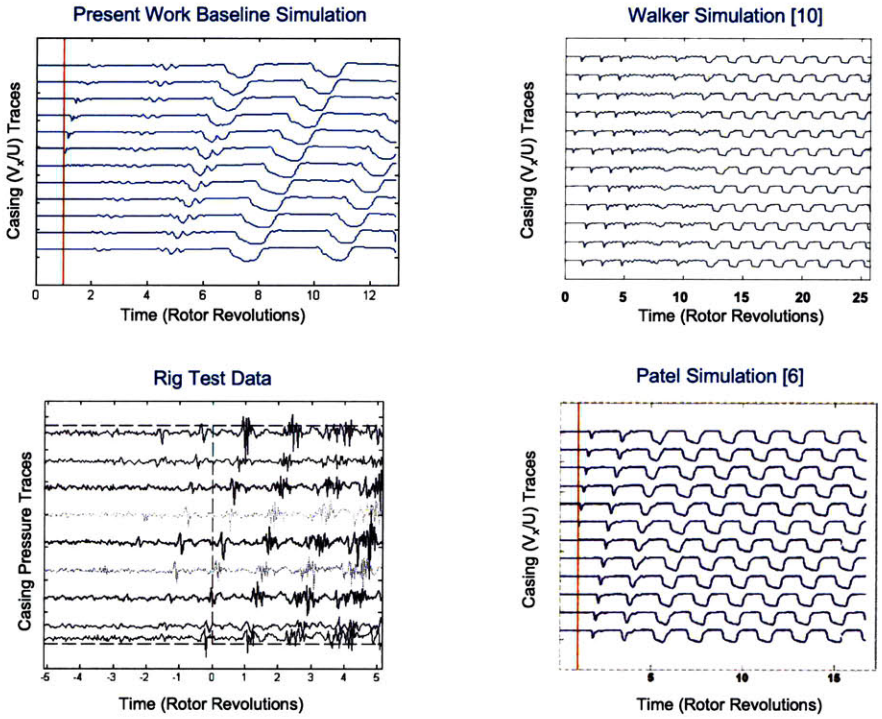

Figure 2-12: Stall onset comparison

Each of the simulations exhibits good agreement with some, but not all aspects of the rig test data. The results from the present work are in good agreement in terms of stall point and inception type, but not cell rotational speed. The results in [6] are in good agreement in terms of inception type and cell rotational speed, but not stall point. The results in [10] are in good agreement in terms of stall point and cell rotational speed, but not inception type. In other words, the increased input fidelity of the present results does not yield an across-the-board increase in output fidelity (as measured against the rig test data), relative to the representations in [10] and [6]. This observation does not imply that the 3D CFD based body force representation is in some way inadequate; rather, it implies that the SLC approach may be adequate. A key caveat, however, is that this comparison is based on the baseline representation. Since SLC and 3D CFD are expected to differ mainly in their ability to capture tip clearance effects (the SLC code used here having no capability in this regard), comparison to the baseline case does not represent a stringent test. A parametric study of rotor end wall forces presented in the next chapter was thus performed to address this point.

Chapter 3

Parametric Study of End Wall Forces

3.1 Motivation

Tip clearance has not been captured as an input in the methodology used to date in this project and a main reason for developing a body force representation from 3D CFD is the potential to address this lack.[1] In this chapter we compare the SLC and the 3D CFD approaches to body forces. The objective is not to develop a tip clearance flow model or to define the effect of tip clearance on computed stall onset, it is rather to evaluate the effect on computed stall onset of a change in force distribution designed to affect the computed pressure rise characteristic in a manner similar to the observed effect of increased tip clearance.

It was shown in [10] that the stall simulation metrics were most sensitive to the radial distribution of forces relative to other inputs. In Chapter 3, the radial distributions in the vicinity of the blade tip are changed relative to the baseline SLC[2] and TBLOCK forces in a way that yields changes to the pressure rise characteristic

[1]This is not the only possible technical approach for capturing the effect of tip clearance, however, and as said an alternative would be to develop a tip clearance flow model for use in conjunction with SLC calculations.

[2]The baseline SLC-based body force representation discussed here is similar to that in [6] described in Table 2.1. There are two differences: the calculations here were for an IGV and rotor, and force-flow reconciliation was employed.

similar to changes with increased tip clearance observed in rig testing.

3.2 Blade Tip Clearance: Trends and Assumptions

Single stage rig tests revealed the following effects of increased tip clearance:

1. Reduced pressure rise capability

   The pressure rise capability of the machine is reduced with increased tip clearance. Off-design, the reduction is more pronounced than it is at design.

2. Increase in stalling flow coefficient

   The stable flow range is reduced by an increase in tip clearance.

The force modifications in this parametric study were chosen to obtain the first of these effects relative to the baseline SLC and TBLOCK cases, respectively. Force modifications were carried out in accordance with the following assumptions:

1. Modifications were implemented as a percent change relative to the baseline local force magnitudes.

2. Radially localized force modifications were introduced in a spanwise region adjacent to the rotor casing whose span-wise extent is approximately seven percent of the annulus height. The force-flow reconciliation procedure was performed on the modified force field, allowing the flow throughout the span to redistribute according to the input force distribution in a consistent manner.

3. Equal changes in axial and tangential forces were applied at all locations throughout the region in which modifications were made. In other words, though the magnitudes of the local forces were modified, the orientations of the local force vectors were not.

4. Equal changes in force were made throughout the axial extent of the spanwise region in which modifications were applied.

3.3 Force Modifications

To obtain reduced pressure rise capability relative to the baseline SLC- and TBLOCK-based simulations, a reduction in the magnitude of the forces radially adjacent to the rotor casing was applied. No changes were made at design, and there was a linear increase with flow decrease. The maximum change corresponded to the off-design operating point. Three variations of force reductions were employed, denoted as Case A, B and C. These corresponded to a 20, 30 and 40 percent maximum reduction relative to the baseline magnitude, respectively.

UnsComp is incapable of accommodating reverse flow in axisymmetric mode. When reverse flow occurs in the UnsComp axisymmetric mode, the reverse flow region grows in axial extent and penetrates the inlet or exit of the computational domain. The occurrence of reverse flow limited the magnitude of the force reductions that could be examined to 40 percent because at a certain threshold magnitude of force reduction, reverse flow in the blade tip region developed. The interpretation of this result is that the inertial and blade forces acting on the volume of fluid in the tip region are incapable of balancing the imposed pressure rise across the blade and a cell of reverse flow develops. The magnitude of the peak reduction was therefore limited to obtain positive flow at all operating points computed in the axisymmetric mode (in the stable flow range).

The reductions in forces used in the parametric study are shown in Figure 3-1. The inset panel shows a meridional view of the UnsComp rotor grid, with the leading and trailing edges marked by red lines. The yellow highlighted region, adjacent to the rotor casing, denotes the cells in which the force modifications were applied. The main panel shows the percentage reduction applied throughout this region (relative to the baseline force values) as a function of overall flow. The four lines denote the baseline case, Case A, Case B and Case C, in which zero, twenty, thirty, and forty percent maximum reductions were applied, respectively. In each of the cases, a linear dependence of percentage reduction on overall flow coefficient was specified, with no reduction at the design operating point and the maximum reduction applied at

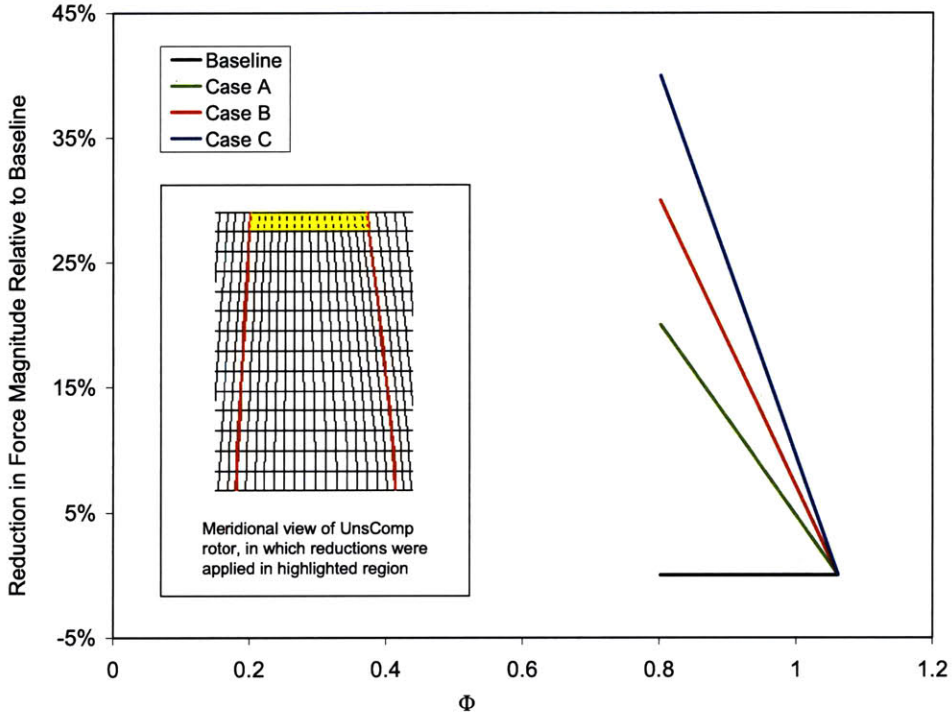

Figure 3-1: Force reductions applied in parametric study

the off-design operating point. This approach was applied in a consistent manner to the baseline SLC- and TBLOCK-based representations; the percentage reduction at a given overall flow for Case A, B and C are the same for the two datasets but the resulting force distributions are different because the baseline SLC and baseline TBLOCK force distributions are different.

The resulting force distributions for the SLC- and TBLOCK-based representations are shown in Figure 3-2. The figure shows the radial distributions of forces resulting from the modifications described in Figure 3-1 at the design and off-design operating points for the SLC- and TBLOCK-based representations. The upper panels correspond to the TBLOCK cases, the lower panels to the SLC cases. For each dataset, the panel on the left shows the radial distribution of the chordwise integrated axial force, and the panel on the right shows the radial distribution of the chordwise

integrated tangential force. In each panel, distributions at the design (dashed black line) and off-design (solid black line) operating points are shown. The distributions for all cases (baseline, A, B and C) are the same at the design operating point for a given representation. This follows from the modifications described in Figure 3-1; the magnitude of the force modifications at design are zero. The off-design distributions, across which there are appreciable differences, are also shown, with color coding for each case (A is green, B is blue and C is red). The differences amongst these cases are confined to the outer span, which also follows from the inset panel in Figure 3-1; the force modifications were limited to the cells adjacent to the rotor casing. For the off-design distributions shown here, it is evident that the Case C distribution, in which the largest off-design modifications were applied, differs most from the baseline distribution. The chordwise-integrated force magnitude is reduced in the outer span relative to the baseline distribution, as expected.

The off-design flow field corresponding to the Case C distribution for the SLC- and TBLOCK-based representations is shown in Figure 3-3. In each of the panels, a meridional pseudocolor plot of the local flow coefficient is shown. The upper panels correspond to the TBLOCK dataset, the lower panels to the SLC dataset. The left panels pertain to the baseline force distributions, the right panels to the Case C distributions. The Case C flow fields exhibit a region of low flow above the blade, qualitatively similar to tip leakage flow, which is not present in the baseline flow fields. This result is consistent with the interpretation that the Case C distributions mimic the effects of increased tip clearance relative to the baseline distributions.

3.4 Computed Pressure Rise Characteristics

The first step in the parametric study was to compute pressure rise characteristics for the reduced force cases. The results are shown in Figure 3-4. The figure summarizes the axisymmetric pressure rise characteristics computed for the cases in the parametric study (baseline, A, B and C) for the SLC and TBLOCK datasets. The left panel shows the TBLOCK cases, the right panel shows the SLC cases. In each

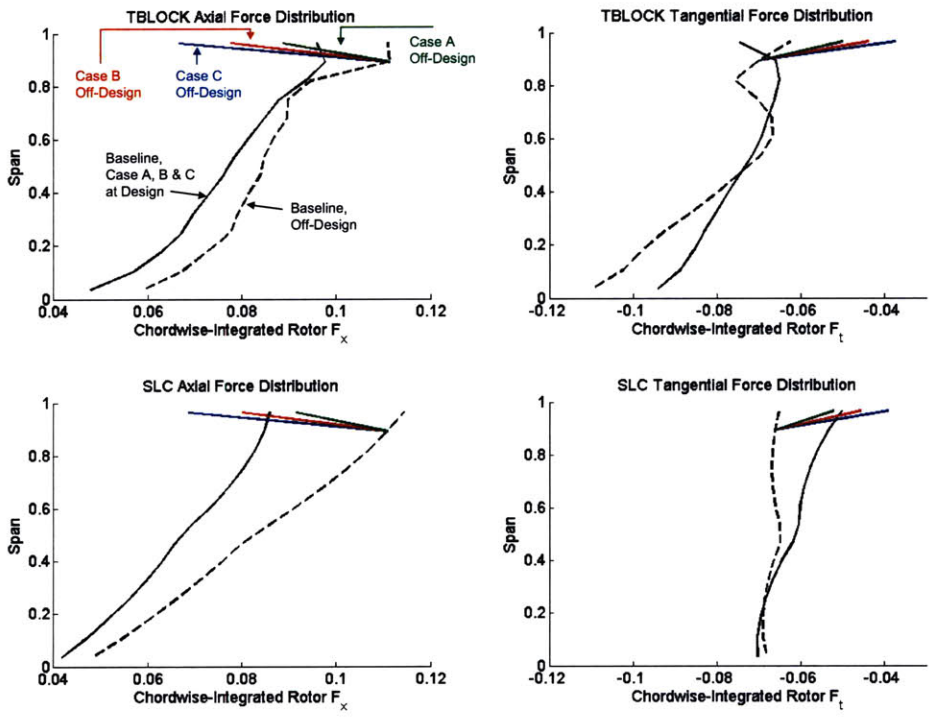

Figure 3-2: Parametric study radial distributions of forces

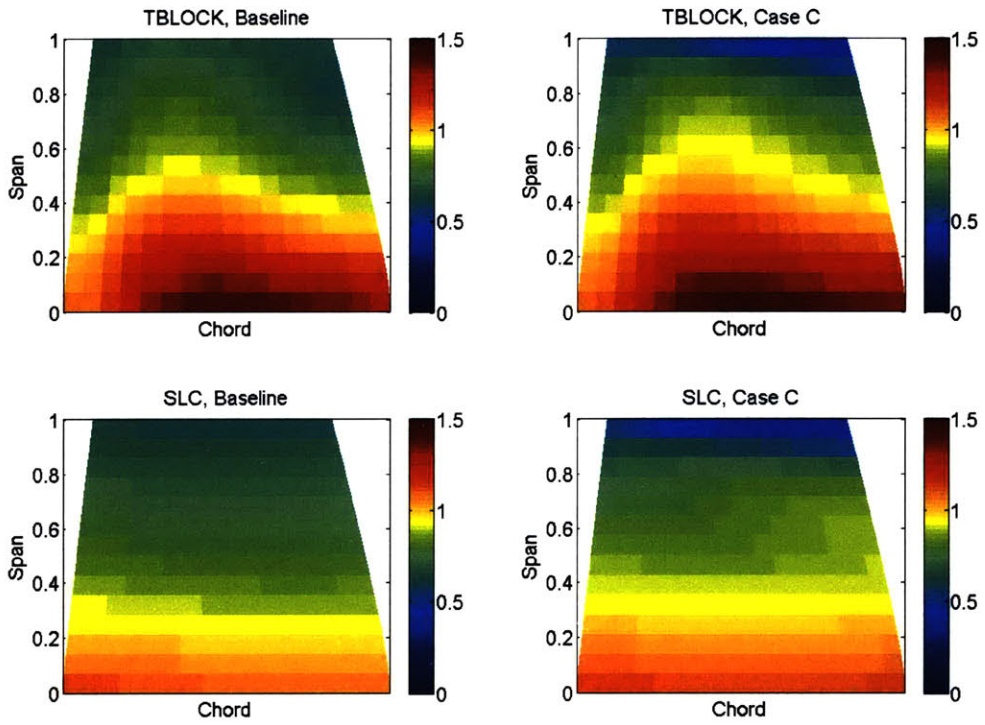

Figure 3-3: Off-design local flow coefficient distributions in rotor

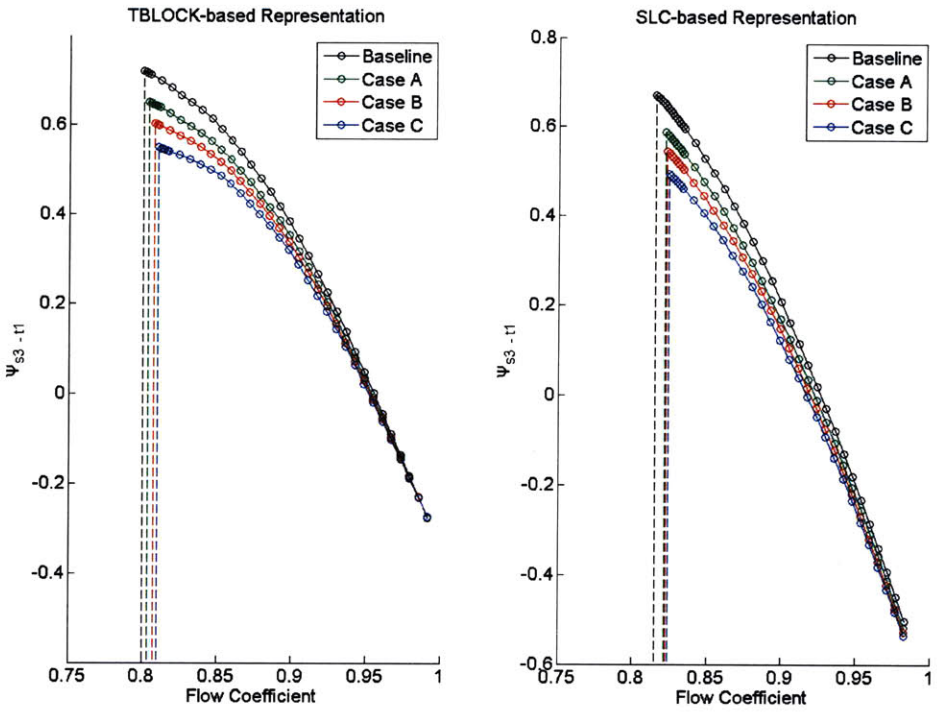

Figure 3-4: Parametric study computed pressure rise characteristics

panel the total-to-static pressure rise characteristics are shown, with color coding corresponding to each case. Furthermore, the instability points (see Figures 3-7 and 3-8 for stall onset results) for each characteristic, which were determined in separate quasi-axisymmetric UnsComp calculations, are denoted by dashed vertical lines for each case. There are two noteworthy features present. First, the trend in pressure rise versus flow for Cases A, B and C relative to the baseline case qualitatively exhibits the measured trend with increased tip clearance discussed in section 3.2. Second, the trend in stalling flow coefficient with Cases A, B and C is consistent with the measured trend with increased tip clearance discussed in section 3.2.

To provide context for the reduction in pressure rise obtained in the computations, the results are compared in Figure 3-5 to empirical tip clearance trends reported in [5], in which reduction in pressure rise is correlated with tip clearance. The chart

depicts the trend in stalling pressure rise versus tip clearance for two sets of empirical data and also shows the 'effective tip clearance' corresponding to the parametric study force distributions. In making the comparison, it was assumed that the baseline SLC- and TBLOCK-based calculations represent a tip clearance of zero. The empirical data includes that given in [5] and two discrete data points from the rig test measurements. The ordinate values for the rig test data points were calculated by multiplying the stalling pressure rise coefficients by the inverse of the normalized stalling pressure rise from the trend in [5] for a tip clearance of 3 percent of annulus height. This locates the '3 percent' rig test point directly on the trend line and locates the '5 percent' point such that a back-to-back comparison to the empirical trend in [5] is possible. The test data exhibits agreement with the trend to within 5 percent, which suggests that the trend is applicable for this compressor.

The additional data points on the chart signify the change in the 'effective tip clearance' from the baseline to the Case C distributions for both the SLC and TBLOCK datasets. The ordinate values for these data points were calculated by multiplying the stalling pressure rise coefficients for the baseline and Case C results by the inverse of the normalized stalling flow coefficient at zero tip clearance from the trend in [5]. The abscissa values were set to zero for the baseline case and determined directly from the trend in [5] for Case C based on the computed ordinate value. Hence the trend was used to estimate the change in 'effective tip clearance' between the baseline and Case C distributions, which was found to be approximately 1 point for both datasets, approximately half of the difference in tip clearance between the test data points.

3.5 Assessment of Relative Sensitivity

The effect of the force reductions on the stall point for the SLC- and TBLOCK-based representations is shown in Figure 3-6. The plot depicts the trend in stalling flow coefficient versus stalling pressure rise coefficient for the SLC- and TBLOCK-based distributions. The flow and pressure rise coefficients are normalized by the respective baseline values for the SLC and TBLOCK datasets. For both datasets, there is a

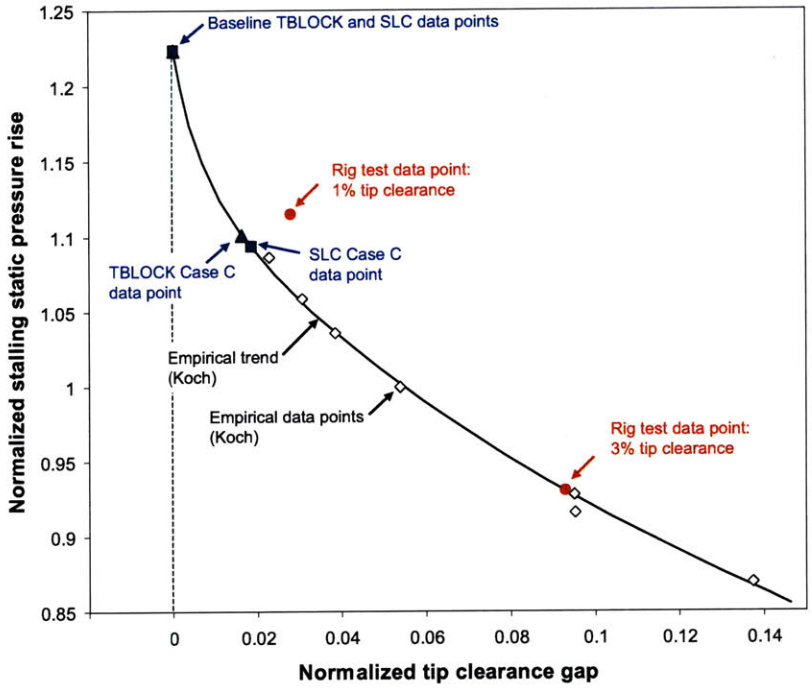

Figure 3-5: Comparison to tip clearance correlation given in [5]

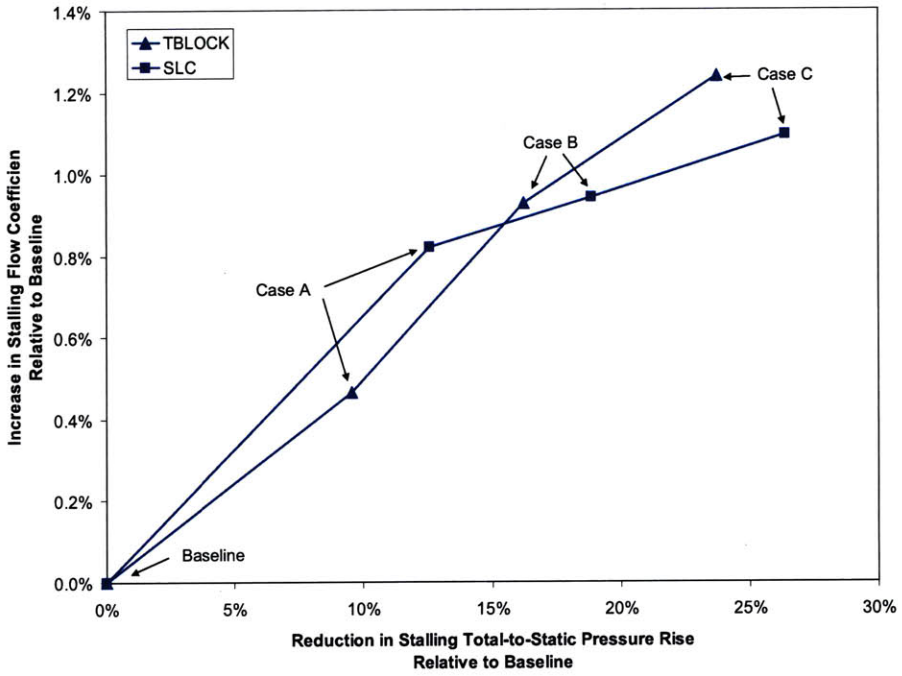

Figure 3-6: Assessment of pressure rise results

change of about 1 percent in stalling mass flow for a change of about 25 percent in stalling pressure rise. The trends show that for a given change in the computed stalling pressure rise (due specifically to a change in the radial distribution of forces near the blade tip), the SLC- and TBLOCK-based calculations yield about the same change in stalling flow coefficient.

3.6 Computed Stall Onset

Stall onset results for the parametric study are shown in Figures 3-7 and 3-8. There are differences in the inception details for the TBLOCK-based computations, evident in the traces spanning the time from 1 to about 5 rotor revolutions for the different cases. However, in terms of 1) inception type 2) the time it takes for the spike to fully

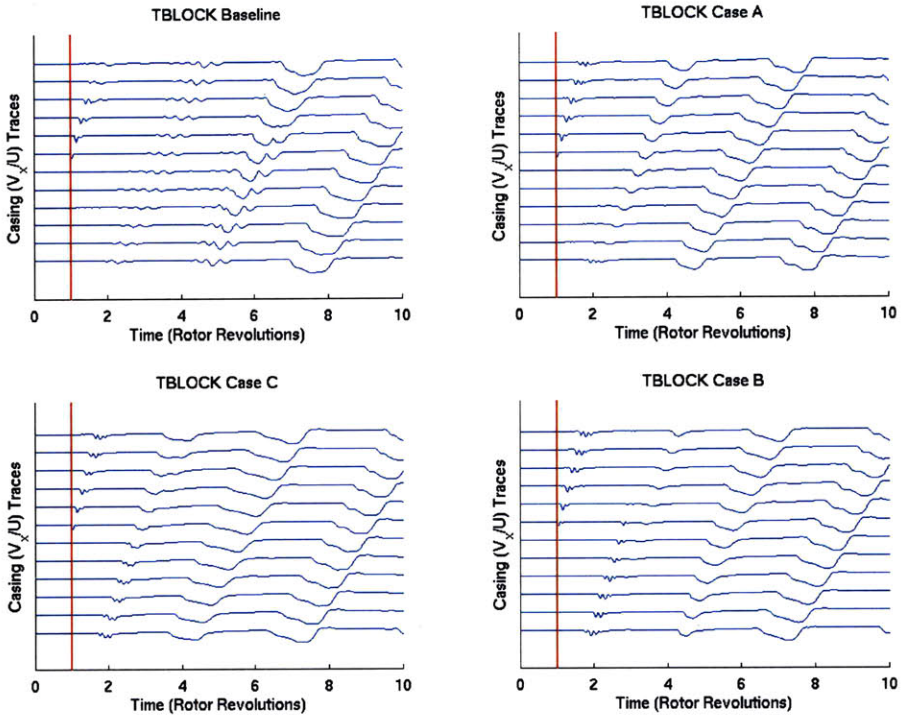

Figure 3-7: Stall onset results for TBLOCK-based baseline and cases A, B, C

develop into a cell and 3) the cell rotational speed, there are no significant differences among the baseline and case A, B and C. Likewise the SLC baseline and Cases A and B yield roughly the same result in those three respects. The SLC-based Case C differs from Case A and B in that the final pattern fully develops in approximately 1 rotor revolution and the resulting cell rotates about the annulus approximately 20 percent faster than in the other cases.

3.7 Parametric Study Conclusions

For the changes to the radial distribution of forces represented by case A, B and C, the stalling flow coefficient versus stalling pressure rise coefficient trend is approximately the same for SLC- and TBLOCK-based body force representations. The trend is

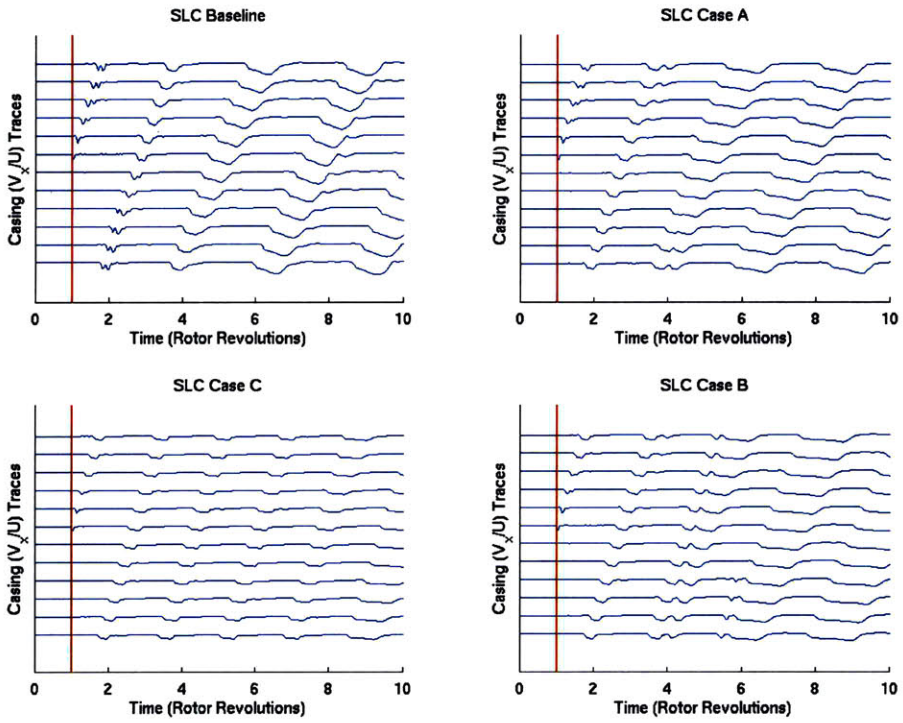

Figure 3-8: Stall onset results for SLC-based baseline and cases A, B, C

roughly linear with a slope of approximately 1 percent difference in stalling mass flow for a 25 percent difference in stalling pressure rise. In other words, for a given change that mimics the effects of increased tip clearance on the stable pressure rise versus flow behavior, the effect on the computed instability point is approximately the same, whether the body force representation derives from SLC or TBLOCK calculations. Furthermore, there are no essential differences in the effect on stall inception between the two datasets. This suggests that if an appropriate tip clearance body force model could be developed for use with SLC-based forces, the increased input fidelity of a body force representation based on 3D CFD may not result in fundamentally different behavior.

Chapter 4

Summary and Conclusions and Future Work

4.1 Summary and Conclusions

This thesis presents three contributions concerning body force representations for use in compressor stall simulations. 1) Body force distributions derived from TBLOCK (3D CFD) calculations are presented and the radial distribution of forces, which is known to be an important factor in stall onset, is compared to the SLC-based distribution. It is shown that the two distributions are in qualitative agreement throughout most of the span, except near the blade tip. 2) Stall onset computations based on the forces extracted from TBLOCK, with an extrapolated distribution of forces in the blade tip region, are presented and compared to SLC-based results. The TBLOCK-based results for stall point and inception type are in good agreement with the test data. The SLC-based computations better agree with the test data in terms of stall cell rotational speed. 3) End wall forces chosen to mimic the effects of increased tip clearance on the pressure rise characteristic were employed in both the TBLOCK- and SLC-based body force representations. For a given change in computed stalling pressure rise due to the assumed end wall forces, the change in computed stalling flow coefficient is approximately the same for the TBLOCK- and SLC-based representations. Further, there are no major differences between the two

datasets in the effect on stall inception.

4.2 Future work

This study implies that a tip clearance model for body forces could be integrated with SLC calculations to produce an SLC-based stability calculation accounting for tip clearance effects. As part of this effort, 3D CFD calculations capable of yielding accurate force distributions in the blade tip clearance region should be undertaken. The forces extracted from 3D CFD could serve as a guide in developing the SLC-based model and also could serve as the basis for stall onset simulations for direct comparison to the SLC-based results.

The areas of future work mentioned above pertain to the overall project goal of producing an accurate stall onset prediction tool with compressor geometry being the sole input and the stall point and inception type being the two outputs. To make progress toward that goal, the tools and methods that have been developed require refinements. In addition to tool-building efforts, it is suggested that additional work focused on the fluid dynamics of stall onset and rotating stall be undertaken on a parallel path. This work would delve into the detailed flow events that constitute compressor stall with an emphasis on understanding what happens and why. The methods described have produced results in general qualitative agreement and in some instances in quantitative agreement with test data. It is the contention here that the methods are now sufficiently proven-out for use in gaining a better understanding of the fluid dynamics at work. Work on the tools should continue, and at the same time the tools should be put to use to broaden the understanding of compressor stall.

Appendices

Appendix A

Clarifications of Prior Work

A.1 Motivation

The goal of this appendix is to clarify aspects of prior work that confounded the author at one point or another throughout this project.

A.2 Control Volume Formulation of Body Force Extraction

A derivation of the body force extraction procedure based on the differential form of the Euler equations and the Divergence Theorem is given in [4]. An equally valid approach that yields the same end result is a control volume analysis, which is perhaps more familiar in the context of computing forces in fluid dynamics and thereby more accessible in terms of interpretation. This section presents a brief summary of the derivation in [4] and then arrives at the same result based on a control volume formulation. For the sake of brevity, only derivations of the axial body force are presented here; the derivations of the radial and tangential components are conceptually identical to that of the axial component.

Starting with [3], all pertinent literature to-date expresses the steady Euler equa-

tions as

$$\frac{\partial \vec{F}}{\partial x} + \frac{\partial \vec{G}}{\partial \theta} + \frac{\partial \vec{H}}{\partial r} = \vec{S} \tag{A.1}$$

where $\vec{F}$, $\vec{G}$ and $\vec{H}$ contain flux terms and $\vec{S}$ contains source terms. In this formulation, the x-components of $\vec{F}$, $\vec{G}$, $\vec{H}$, and $\vec{S}$ are

$$F_x = (\rho V_x^2 + rP)r\lambda \tag{A.2a}$$

$$G_x = (\rho V_x V_\theta)r\lambda \tag{A.2b}$$

$$H_x = (\rho V_x V_r)r\lambda \tag{A.2c}$$

$$S_x = \lambda r \rho \mathbb{F}_x + rP\frac{\partial \lambda}{\partial x} \tag{A.2d}$$

where $\mathbb{F}_x$ is the axial body force [1]. The formulation of the governing equations in [3] involves a rearrangement of the commonly expressed mass and momentum equations (see [4] for a step-by-step description of the algebra involved), and it can also be derived directly from differential considerations [9]. For a time- and theta-averaged flow, the body force extraction procedure in [4] entails evaluating the derivatives of $\vec{F}$ and $\vec{H}$ (the theta-derivative of $\vec{G}$ is not evaluated because it is zero by definition for a theta-averaged flow), and equating the sum of the derivatives to the corresponding source term. The resulting expression is then manipulated to obtain the body force.

In the context of this project, the body force is always extracted for a discrete axisymmetric cell in the computational domain and then normalized by the mass of fluid in the cell volume. The cross-section of a typical cell with flux terms $\vec{F}$ and $\vec{H}$ defined on each face is shown in Figure A-1. In the formulation in [4], the theta-extent of the cross-section shown in Figure A-1 is 360 degrees. For the control volume geometry shown, the x- and r-derivatives in Equation A.1 can be computed from the fluxes defined on each face by use of the Divergence Theorem. For the x-component,

[1] In prior literature, F_x denotes the axial body force. To avoid any confusion between the axial component of the flux variable $\vec{F}$ and the axial component of the body force, $\mathbb{F}_x$ is used here and throughout this document.

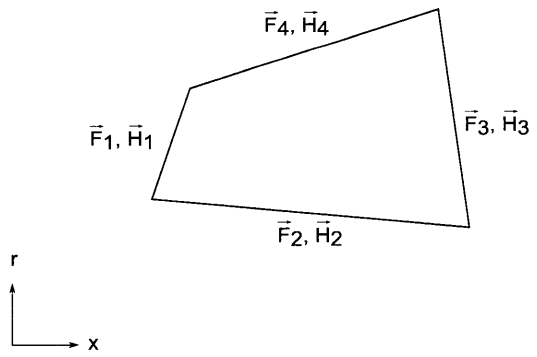

Figure A-1: Meridional control volume geometry

the derivatives are given by

$$\frac{\partial F_x}{\partial x} = \frac{-F_{1_x}A_{1_{axial}} - F_{2_x}A_{2_{axial}} + F_{3_x}A_{3_{axial}} - F_{4_x}A_{4_{axial}}}{Volume_{cell}} \tag{A.3a}$$

$$\frac{\partial H_x}{\partial r} = \frac{H_{1_x}A_{1_{radial}} - H_{2_x}A_{2_{radial}} + H_{3_x}A_{3_{radial}} + H_{4_x}A_{4_{radial}}}{Volume_{cell}} \tag{A.3b}$$

where $A_{1_{axial}}$ denotes the axial area of face 1 based on a theta-extent of 360 degrees, $A_{1_{radial}}$ denotes the radial area of face 1 (again based on 360 degrees), and so on; $Volume_{cell}$ denotes the cell volume based on a 360 degree theta-extent.[2] Combining Equations A.1, A.2 and A.3, the axial body force can be expressed as

$$\mathbb{F}_x = \frac{(-\lambda r A_{axial}(\rho V_x^2 + P))_1 - (\lambda r A_{axial}(\rho V_x^2 + P))_2 + (\lambda r A_{axial}(\rho V_x^2 + P))_3 - (\lambda r A_{axial}(\rho V_x^2 + P))_4}{(\lambda r \rho Volume)_{cell}}$$
$$+ \frac{(\lambda r \rho V_x V_r A_{radial})_1 - (\lambda r \rho V_x V_r A_{radial})_2 + (\lambda r \rho V_x V_r A_{radial})_3 + (\lambda r \rho V_x V_r A_{radial})_4}{(\lambda r \rho Volume)_{cell}} - \left(\frac{rP\frac{\partial \lambda}{\partial x}}{\lambda r \rho}\right)_{cell} \tag{A.4}$$

The theta- and r-components of the blade force are calculated in a similar manner. Some of the terms in Equation A.4 are familiar in the context of control volume analyses, but there are some unfamiliar coefficients. Also the term that includes

[2]The signs of some of the terms in Equation A.3 (and the equations that follow from it) differ from those in [4]. The difference is due to a different sign convention; conceptually, the statements are identical.

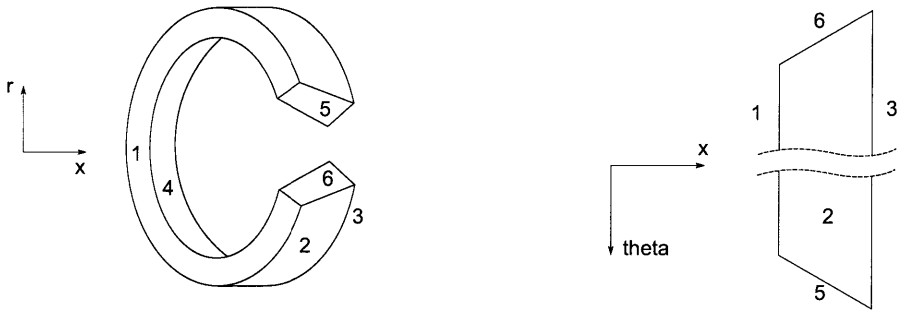

(a) 3D control volume geometry

(b) Top-down view of 'unrolled' control volume in the x- and theta-plane

Figure A-2: Alternative meridional control volume geometry

$\frac{\partial \lambda}{\partial x}$ is unfamiliar. It is possible to derive Equation A.4 purely from control volume considerations and in doing so to address the physical meaning of each term and coefficient.

To begin with, consider the control volume shown in Figure A-2. The cross-section of this control volume is identical to that shown in Figure A-1, but the geometries are otherwise different in that the control volume in Figure A-2 accounts for metal blockage, while that in Figure A-1 does not. Metal blockage can be interpreted as a direct reduction in the circumferential extent of an annulus (for example, a metal blockage of 0.8 would imply a reduction of 20 percent in the circumferential extent). For the geometry shown in Figure A-2, the metal blockage is larger at the leading edge than at the trailing edge. That is why faces 5 and 6 are skewed (i.e., the face surfaces are not on constant-theta planes). No flux can pass through faces 5 and 6, but pressure forces do act on those faces.

The underlying assumption in the body force extraction methodology is that any imbalance in the net pressure force and the net momentum flux is due to a body force imparted by the blade. The x-component of the pressure force and momentum flux for each face of the control volume in Figure A-2 is tabulated in Table A.1. The face areas listed in Table A.1 are the same as those in Equation A.3 (they denote areas on a 360 degree theta basis). The blockage coefficients are thus required for the areas

Table A.1: Bookkeeping of pressure forces and momentum fluxes

Face	X-Component of Pressure Force	X-Component of Momentum Flux
1	$(+P\lambda A_{axial})_1$	$(-\rho V_x^2 \lambda A_{axial} + \rho V_x V_r \lambda A_{radial})_1$
2	$(+P\lambda A_{axial})_2$	$(-\rho V_x^2 \lambda A_{axial} - \rho V_x V_r \lambda A_{radial})_2$
3	$(-P\lambda A_{axial})_3$	$(+\rho V_x^2 \lambda A_{axial} + \rho V_x V_r \lambda A_{radial})_3$
4	$(+P\lambda A_{axial})_4$	$(-\rho V_x^2 \lambda A_{axial} + \rho V_x V_r \lambda A_{radial})_4$
5	$(+P\lambda A_{axial})_5$	none
6	$(+P\lambda A_{axial})_6$	none

Table A.2: Contributions of fluxes and pressures at each face to the blade force

Face	Body Force Imparted by Blade
1	$((-\rho V_x^2 - P)\lambda A_{axial} + \rho V_x V_r \lambda A_{radial})_1$
2	$((-\rho V_x^2 - P)\lambda A_{axial} - \rho V_x V_r \lambda A_{radial})_2$
3	$((+\rho V_x^2 + P)\lambda A_{axial} + \rho V_x V_r \lambda A_{radial})_3$
4	$((-\rho V_x^2 - P)\lambda A_{axial} + \rho V_x V_r \lambda A_{radial})_4$
5	$(-P\lambda A_{axial})_5$
6	$(-P\lambda A_{axial})_6$

to be consistent with the geometry shown in Figure A-2.

The integral form of the momentum equation states that the sum of the x-component of the forces acting on the control volume equals the net flux of x-momentum out of the control volume. In this case, the forces acting on the control volume include only the pressure forces and the body force imparted by the blade. Table A.1 can be reformulated to express the difference of the momentum flux and pressure force for each face, which is equivalent to the blade force acting on each face. The total blade force is then equal to the sum of the rows of this reformulated table (see Table A.2). Since the pressure on faces 5 and 6 is the same as the pressure at the cell center (recall that the flow has been theta-averaged prior to this control volume analysis), the contribution from face 5 and 6 can be expressed as

$$(-P\lambda A_{axial})_5 = (-P\lambda A_{axial})_6 = -\frac{1}{2} P_{cell} \overline{A}_{axial} (\lambda_3 - \lambda_1) \tag{A.5}$$

where $\overline{A}_{axial}$ denotes the average of $A_{1_{axial}}$ and $A_{3_{axial}}$. A further simplification can be made by normalizing Equation A.5 by the mass of fluid in the control volume,

Table A.3: Normalized contributions of fluxes and pressures at each face to the blade force

Face	Normalized Body Force Imparted by Blade
1	$\frac{((-\rho V_x^2 - P)\lambda A_{axial} + \rho V_x V_r \lambda A_{radial})_1}{(\rho\lambda Volume)_{cell}}$
2	$\frac{((-\rho V_x^2 - P)\lambda A_{axial} - \rho V_x V_r \lambda A_{radial})_2}{(\rho\lambda Volume)_{cell}}$
3	$\frac{((+\rho V_x^2 + P)\lambda A_{axial} + \rho V_x V_r \lambda A_{radial})_3}{(\rho\lambda Volume)_{cell}}$
4	$\frac{((-\rho V_x^2 - P)\lambda A_{axial} + \rho V_x V_r \lambda A_{radial})_4}{(\rho\lambda Volume)_{cell}}$
5	$-\frac{1}{2}\left(\frac{P\frac{\partial\lambda}{\partial x}}{\lambda\rho}\right)_{cell}$
6	$-\frac{1}{2}\left(\frac{P\frac{\partial\lambda}{\partial x}}{\lambda\rho}\right)_{cell}$

$(\rho\lambda Volume)_{cell}$:

$$\frac{-\frac{1}{2}P_{cell}\overline{A}_{axial}(\lambda_3 - \lambda_1)}{(\rho\lambda Volume)_{cell}} = -\frac{1}{2}\left(\frac{P\Delta\lambda}{\lambda\rho\Delta x}\right)_{cell} = -\frac{1}{2}\left(\frac{P\frac{\partial\lambda}{\partial x}}{\lambda\rho}\right)_{cell} \tag{A.6}$$

Table A.3 lists all the terms from Table A.2, normalized by the mass of fluid in the control volume. Summing the rows in Table A.3, it is evident that the result is identical to Equation A.4. Hence it has been shown that a control volume approach yields the same result as that in [4]. The initially unfamiliar coefficients and metal blockage derivative term in the expression from [4] have been shown to be intuitively related to the control volume geometry. Metal blockage gives rise to inclined faces of the control volume which in turn contribute forces to the analysis.

A.3 Quasi-Axisymmetric Compressor Model

In prior work, the UnsComp instability computations have been described as 'locally axisymmetric' [3]. The current view is that 'quasi-axisymmetric' is a more precise description. A key feature of the model in [3] is that although the blade forces are extracted from an axisymmetric flow field and are tabulated based on axisymmetric flow properties, they are not applied in an axisymmetric manner in the Euler solver. The Euler solver applies a body force on each computational cell based on the local flow properties known at each cell. When a force perturbation is input, this allows

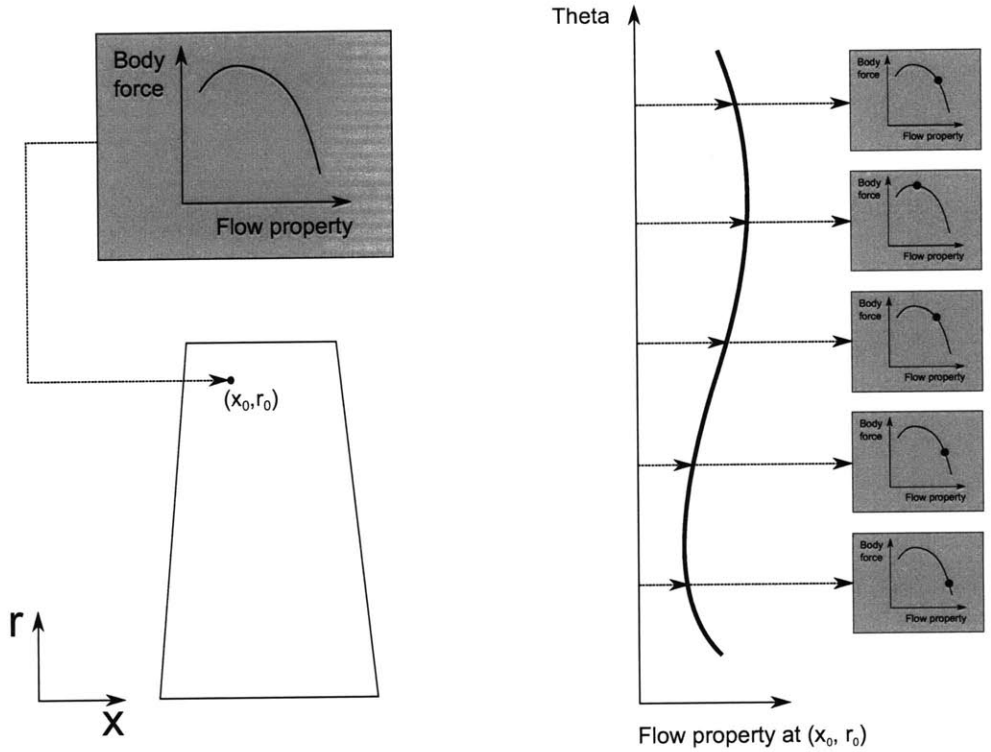

Figure A-3: Depiction of the quasi-axisymmetric body force model

non-axisymmetric flow to develop (which is required for stall inception to occur) because the cells in the region of the perturbation respond to the change in local flow properties. In other words, each cell at a given radius and axial location is subject to a fixed relationship between flow properties and body forces, but there can be a circumferential variation in the body forces acting on those cells due to a circumferential variation in local flow properties. 'Quasi' means 'as if'; in essence, each cell in the domain responds to the local flow properties as if they were the axisymmetric flow properties. Hence it is thought that 'quasi-axisymmetric' is more precise than 'locally axisymmetric' as a description of the model. Figure A-3 depicts the quasi-axisymmetric nature of the model in [3].

A.4 Discussion of Walker's [10] Results

There are several caveats pertinent to these results. The first is, that when the radial distribution of rotor axial and tangential forces were changed, the total rotor axial or tangential force were not constrained to remain constant. Due to the annular geometry of an axial compressor, a percentage increase or decrease in force at the tip is not equivalent to the same percent increase or decrease at the hub. Due to the larger radius, the tip forces have a proportionally larger contribution to the total rotor force. As a result, both the total force and the radial distribution of the force were varied. Second, the chordwise-integrated body forces for each blade row were computed from SLC calculations, which provide no information about the flow interior to each blade row. These were axially distributed to obtain a discrete force value at each chordwise location in each blade row. These forces were tabulated against the local flow coefficient obtained from the SLC calculation, which were assumed to be constant for all chordwise locations in each blade row. However, within each blade row, the force varied from the leading edge to the trailing edge, but the local flow coefficients corresponding to those forces did not. As a result, as discussed in 2.6 the forces and flow variables are not self-consistent. This was also true for the modification of the rotor body forces in the sensitivity study. To generate a set of self-consistent local force and local flow values, the force-flow reconciliation procedure described in 2.6 would need to be implemented.

Bibliography

[1] CAMP, T., AND DAY, I. A study of spike and modal stall inception in a low-speed axial compressor. *ASME Journal of Engineering For Power 120* (July 1998), 393–401.

[2] DENTON, J. Tblock-07.5: Multiblock flow solver, August 2007.

[3] GONG, Y. *A Computational Model for Rotating Stall and Inlet Distortions in Multi-Stage Compressors.* Phd thesis, Massachusetts Institute of Technology, February 1999.

[4] KIWADA, G. Development of a body force description for compressor stability assessment. Master's thesis, Massachusetts Institute of Technology, February 2008.

[5] KOCH, C. Stalling pressure rise capability of axial flow compressor stages. *ASME Journal of Turbomachinery 103* (October 1981), 645–656.

[6] PATEL, A. Assessment of a body force representation for compressor stability estimation. Master's thesis, Massachusetts Institute of Technology, June 2009.

[7] PATEL, A. Personal communication. June 2009.

[8] REICHSTEIN, G. Estimation of axial compressor body forces using three-dimensional flow computations. Master's thesis, Massachusetts Institute of Technology, February 2009.

[9] TAN, C. Notes by c. s. tan on blade-gap averaging flow equations and blade-metal blockage. April 2009.

[10] WALKER, T. K. The development and requirements of a body force databse from two-dimensional and streamline curvature calculations. Master's thesis, Massachusetts Institute of Technology, February 2009.